SECOND LAW ANALYSIS OF A PASSIVE MICROMIXER

WITH FLOW OBSTACLES

A Thesis

By

Steven E. Ferguson, Jr.

Presented to the Jackson College of Graduate Studies of the University of Central Oklahoma in Partial Fulfillment of the Requirements for the Degree of

MASTER OF SCIENCE IN ENGINEERING PHYSICS – MECHANICAL ENGINEERING

MAY, 2020

SECOND LAW ANALYSIS OF A PASSIVE MICROMIXER WITH FLOW OBSTACLES

By
Steven E. Ferguson, Jr.

5/7/2020

Jackson College of Graduate Studies at the University of Central Oklahoma

A THESIS APPROVED FOR

THE DEPARTMENT OF ENGINEERING AND PHYSICS

By

_____

Committee Chairperson

_____

Committee Member

_____

Committee Member

Abstract

Passive micromixers focus on variations in the channel geometry and the presence of flow obstacles as a means of improving mixing efficiency. An analysis of these geometries can provide useful information for further mixer design iteration. These passive micromixers have applications in biosciences, in particular as point-of-care diagnostic testing devices. Because these mixers utilize the channel geometry, rather than moving parts, to increase mixing efficiency, they can be more easily deployed in developing or relatively undeveloped locales.

This thesis presents a detailed computational analysis of a channel design that utilizes obstacles that split and recombine the fluid flow in a rectangular microchannel. Numerical simulations were created using computational fluid dynamics software running on a supercomputer cluster. The Second Law of Thermodynamics is utilized to identify areas of irreversibility due to both chaotic advection induced by flow obstacles and diffusion. The design is analyzed for a range of Reynolds numbers typical to micromixers. Additionally, different inlet velocity ratios are analyzed to examine whether this can potentially improve mixing efficiency within this channel design.

Acknowledgement

I would like to first offer my eternal gratitude to my parents, whose love and support enabled me to continue my formal education long past the point when it would have otherwise ended. This, finally, is the end of that road (at least for now). Three degrees is more than enough for me; learning never truly ends.

Without the abetment of my thesis advisor Dr. Evan Lemley, this thesis would certainly never have come to fruition. I owe a big thanks to him for his years of mentoring and putting up with my slow but steady progress.

Finally, I'd like to thank my friends for their none-too-gentle ribbing, which has served as extra motivation to finish this thesis. Fellow graduates and post-graduates of the group have provided a valuable pool of confidants regarding the graduate experience. A special thanks goes to Jeremy Spohn, whose gift of a laptop roughly a year ago enabled me to continue work on this thesis during the three weeks of this April that my desktop computer was suffering from critical component failures.

I would be remiss not to acknowledge the corona virus pandemic affecting the world as of this writing. As a result, the last nine weeks' worth of work on this thesis were done without ever returning to campus or having an in-person meeting with anyone from the university. Even the defense was held online. I again thank Dr. Lemley for his aid via email and being willing to meet virtually for consultations.

Table of Contents

List of Tables and Figures

Nomenclature

Latin Symbols	
C	Concentration
D	Diffusion constant
$\dfrac{D}{Dt}$	Total Derivative
K	Turbulent kinetic energy
k_B	Boltzmann's constant
MI	Mixing Index
N	Avogadro's constant
P	Fluid pressure
R	Ideal gas constant
r	Particle radius
$\dot{S}$	Entropy Generation Rate
T	temperature
t	Time
u	Flow velocity
u	x-direction velocity
v	y-direction velocity
w	z-direction velocity
x	Longitudinal axis
y	Vertical axis
z	Transverse axis

Greek symbols	
∇	Gradient
∇^2	Laplacian operator
μ	Dynamic viscosity
ϵ	Rate of dissipation of turbulent kinetic energy
ν	Kinematic viscosity μ/ρ
π	3.14159…
ρ	Fluid density
σ	Effective Prandtl number
σ^2	variance

Subscripts	
F	Frictional part
T	Temperature part or Total
D'	Indirect (turbulent) dissipation

Chapter 1: Introduction

Microfluidic devices such as passive micromixers have increasing application in the biosciences area and may be used as part of point-of-care diagnostic testing devices, which are becoming common-place in developing locales [1]. In these locations, microfluidic devices offer affordable and portable alternatives to larger-scale devices. These diagnostic applications can combine highly sensitive biosensor designs with the fluidic manipulation made available by lab-on-a-chip (LOC) microfluidic systems [2]. For example, one such device is able to detect foodborne pathogens via one of several detection methods including a process called polymerase chain reaction (PCR), in which a low concentration of analyte is amplified via specific nucleic acids or a thermocycling process in order to enable easier detection of targeted pathogens [3]. Characterizing and improving the mixing efficiency of these microfluidic devices is an ongoing effort and the focus of this research.

1.1: Micromixer Background

Micromixers can be classified as being either active or passive [4]. Active mixing utilizes some mechanical or electromagnetic means of causing the fluids to interact [5]. Some active mechanical designs that employ moving parts are difficult to implement on the microscale. Electromagnetically driven devices are not suitable for point-of-care diagnostic and many other applications. Active mixers were not investigated in this study. Passive micromixers rely on channel geometry to increase mixing effectiveness by increasing chaotic advection and diffusion as the primary means of mixing. Diffusion is a function of time and contact area [6]. Generally, mixing via diffusion can be increased with longer residence times and the injection of multiple layers of fluids to increase contact area [7]. Chaotic advection occurs when the channel geometry

1

directs the lamination layers back upon themselves to force interaction. This study is primarily focused on a mixer design that involves repeatedly separating and recombining the fluid flow to increase chaotic advection.

Micromixers that rely on repeatedly separating and recombining the fluid flow have been studied both experimentally and numerically by many researchers, and it has been found that these micromixers have a significant effect on performance in terms of decreased power requirements [8]. Performance is also strongly affected by the fact that the fluid flow is laminar due to low Reynold's numbers [5]. In the laminar flow regime, mixing is mostly limited to molecular diffusive mixing if chaotic advection is not enhanced [9, 4, 10, 11].

Chaotic advection can be utilized to encourage mass transfer which increases the efficiency of micromixers. These interactions can be encouraged by the design of the channel's geometry, which can cause the flow to fold [12], split and recombine [9, 13], or stretch [9, 12]. Flow geometries have included obstacles [14, 15] and complicated two- [16] and three-dimensional geometries [17, 18, 19, 20, 21]. Chaotic advection can also be promoted by varying the inlet flow ratios [22].

Diffusion is the other principal form of passive mixing. It utilizes the tendency of particles to migrate from areas of higher concentration to areas of lower concentration via random fluctuations in their motion known as Brownian movement [23]. Diffusion can be enhanced by increasing the contact area of the mixing fluids. Lamination is one of the two primary methods of increasing the contact area between the fluids [7]. Lamination splits the flow into sub-streams and then recombines them. This increases the number of faces of contact between the fluid

species. Injection is the other method of increasing the contact area by forcing one fluid transverse to the flow of the other fluid [24].

Micromixers can be characterized using the values of the Reynolds number of the flow [25] and the entropy generation within the device [26]. Entropy generation characterizes the irreversibility of the system. Locations within the model that demonstrate a higher entropy generation can be used to identify locations where the geometry is promoting more mixing [27].

1.2: Objectives

In this thesis, irreversibilities due to viscous fluid dissipation and diffusive motion between two mixing fluids are predicted by modeling the fluid flow and subsequently determining the entropy generated due to these irreversibilities. The Second Law of Thermodynamics predicts entropic increase [28]; while this thesis created simulations using computational fluid dynamics (CFD) software, a Second Law Analysis (SLA) is conducted upon those models. This study investigates the relative entropy generation rates with varying Reynolds numbers (a dimensionless quantity that provides a ratio of the internal forces to viscous forces within a fluid at a given flow rate [25]) in a micro-scale mixing geometry with square-shaped obstacles. Unlike many previous studies, this thesis focused not only on the chaotic advective motion of the mixing fluids, but also on the diffusion of the unmixed fluids into each other [9, 29, 30].

This work is focused on numerical simulations of flow in a particular mixer design (henceforth called simply 'the model') conducted using CFD software running on a supercomputer cluster. This enabled the testing of a wide range of flows with varying Reynolds numbers. A variety of mesh densities are also investigated to ensure that CFD results could be verified.
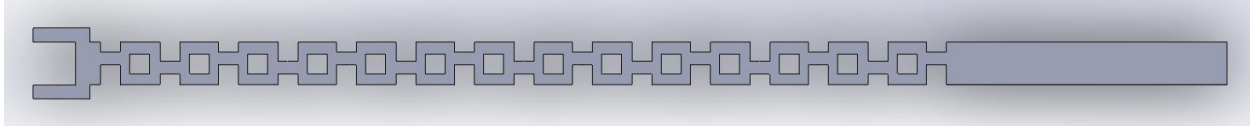
Figure 1: The Model Geometry

The examination of this mixer includes an analysis of its shapes and obstacles and the secondary flows they induce, and whether those flows contribute to overall entropy generation and, by extension, passive mixing. Variations on the flow parameters, notably on different inlet velocities, are also examined for improved mixing.

This thesis seeks to determine a relationship among several relevant quantities in the selected micromixer design, which features square obstacles to split and recombine the flow. Using a model created with SOLIDWORKS®, the design will be used to run a series of simulations with a variety of input Reynolds numbers commonly used in microfluidic devices (from 0-500) and then analyzed using VisIt [31] post-processing tools. Reynolds number, entropy generation rate, mixing efficiency, and inlet velocity ratios will all be examined and analytical relationships between these quantities will be sought. Using work from this thesis, the goal is to improve future micromixer designs by identifying geometric features, flow ratios, and other quantities that can help to increase mixing efficiency.

Chapter 2: Theoretical Background

In modeling dynamic fluid processes via computer models, is it important to understand the physical laws that are used to model fluid flow. The conservation of both mass and momentum are central to the formulation of fluid dynamics.

The conservation of mass can be expressed in a fluid via what is commonly called the Continuity Equation [25].

$$\frac{\partial \rho}{\partial t} + \nabla \cdot (\rho \mathbf{u}) = 0. \tag{2.1}$$

The conservation of momentum is represented by the Navier-Stokes Equation [25] for constant viscosity and density (ie: for an incompressible fluid)

$$\rho \frac{\partial \mathbf{u}}{\partial t} + \rho \mathbf{u} \cdot \nabla \mathbf{u} = -\nabla P + \mu \nabla^2 \mathbf{u}. \tag{2.2}$$

Note that Equations 2.1 and 2.2 can be used for all incompressible constant viscosity flows, including the laminar and turbulent flow regimes. Turbulent flows are more easily modeled with both an energy transport equation and a second equation that models the rate of change of either dissipation ϵ or turbulent length scales L. In this study, we used the former, utilizing the K-ϵ model for turbulent flows. The two equations for that model are

$$\frac{DK}{Dt} \approx \frac{\partial}{\partial x_j}\left(\frac{\nu_t}{\sigma_K}\frac{\partial K}{\partial x_j}\right) + \nu_t \frac{\partial \bar{u}_i}{\partial x_j}\left(\frac{\partial \bar{u}_i}{\partial x_j} + \frac{\partial \bar{u}_j}{\partial x_i}\right) - \epsilon \tag{2.3}$$

and

$$\frac{D\epsilon}{Dt} \approx \frac{\partial}{\partial x_j}\left(\frac{\nu_t}{\sigma_\epsilon}\frac{\partial \epsilon}{\partial x_j}\right) + C_1 \nu_t \frac{\partial \bar{u}_i}{\partial x_j}\left(\frac{\partial \bar{u}_i}{\partial x_j} + \frac{\partial \bar{u}_j}{\partial x_i}\right) - C_2 \frac{\epsilon^2}{K} \tag{2.4}$$

with

$$\nu_t \approx \frac{C_\mu K^2}{\epsilon}. \tag{2.5}$$

These equations contain five empirical constants that have the following recommended values:

$$C_\mu = 0.09 \quad C_1 = 1.44 \quad C_2 = 1.92 \quad \sigma_K = 1.0 \quad \sigma_\epsilon = 1.3.$$

These are not universal and must be modified for cases involving features such as jets, wakes, or recirculating flows, but can be used for general cases such as were employed in this thesis [25].

In an effort to quantify the quality of the resultant mixture, we also develop a mixing index (MI). This index relies upon the variance of the concentrations of the two fluids at a plane normal to the flow direction within a given device [32, 33, 34]. The variance can be found with the equation

$$\sigma^2 = \sqrt{\frac{1}{N}\sum_{i=1}^{N}(C_i - \bar{C})^2}. \tag{2.6}$$

The Mixing Index is then defined based on the variance on that plane and the maximum possible variance, which would occur in a completely unmixed solution.

$$MI = 1 - \sqrt{\frac{\sigma^2}{\sigma_{max}^2}}. \tag{2.7}$$

A Second Law Analysis (SLA) involves characterizing a flow using entropy generation rates and the Second Law of Thermodynamics. Entropy generation occurs in mechanical systems due to friction, unrestrained expansion, heat transfer, and mixing [35]. In this work friction is due to viscous shear stresses in a flowing fluid and mixing of two fluids. An SLA may be performed

theoretically by knowing the continuous fluid velocity field and concentration gradients. In this work, in which computer simulations are performed, discrete versions of the velocity field and concentration gradients will be used to calculate entropy generation rates.

The entropy generation field in Cartesian coordinates can be expressed in two parts [36, 37, 38]. The viscous or frictional part is:

$$\dot{S}_F{}''' = \frac{\mu}{T_o}\left[2\left(\left(\frac{\partial u}{\partial x}\right)^2 + \left(\frac{\partial v}{\partial y}\right)^2 + \left(\frac{\partial w}{\partial z}\right)^2\right) + \left(\frac{\partial u}{\partial y} + \frac{\partial v}{\partial x}\right)^2 + \left(\frac{\partial u}{\partial z} + \frac{\partial w}{\partial x}\right)^2 + \left(\frac{\partial v}{\partial z} + \frac{\partial w}{\partial y}\right)^2\right)\right]. \quad (2.8)$$

The thermal part is:

$$\dot{S}_T{}''' = \frac{K}{T_o^2}\left[\left(\frac{\partial T}{\partial x}\right)^2 + \left(\frac{\partial T}{\partial y}\right)^2 + \left(\frac{\partial T}{\partial z}\right)^2\right]. \quad (2.9)$$

These can be combined with another portion that describes the volumetric entropy generation rate associated with concentration gradients, which yields:

$$\dot{S}''' = \dot{S}_F''' + \dot{S}_T''' + \frac{RD}{C_o}\left[\left(\frac{\partial C}{\partial x}\right)^2 + \left(\frac{\partial C}{\partial y}\right)^2 + \left(\frac{\partial C}{\partial z}\right)^2\right]$$
$$+ \frac{RD}{T_o}\left[\left(\frac{\partial T}{\partial x}\right)\left(\frac{\partial C}{\partial x}\right) + \left(\frac{\partial T}{\partial y}\right)\left(\frac{\partial C}{\partial y}\right) + \left(\frac{\partial T}{\partial z}\right)\left(\frac{\partial C}{\partial z}\right)\right]. \quad (2.10)$$

This can be simplified for the purposes of this thesis, which examines isothermal cases. We first define $\dot{S}_D'''$, which is the diffusive component of Equation 2.10, above, as:

$$\dot{S}_D''' = \frac{RD}{C_o}\left[\left(\frac{\partial C}{\partial x}\right)^2 + \left(\frac{\partial C}{\partial y}\right)^2 + \left(\frac{\partial C}{\partial z}\right)^2\right]. \quad (2.11)$$

We then obtain for this work

$$\dot{S}''' = \dot{S}_F''' + \dot{S}_D''' \quad (2.12)$$

$$\dot{S}''' = \frac{\mu}{T_o} \left[2 \left(\left(\frac{\partial u}{\partial x} \right)^2 + \left(\frac{\partial v}{\partial y} \right)^2 + \left(\frac{\partial w}{\partial z} \right)^2 + \left(\frac{\partial u}{\partial y} + \frac{\partial v}{\partial x} \right)^2 + \left(\frac{\partial u}{\partial z} + \frac{\partial w}{\partial x} \right)^2 + \left(\frac{\partial v}{\partial z} + \frac{\partial w}{\partial y} \right)^2 \right) \right]$$
$$+ \frac{RD}{C_o} \left[\left(\frac{\partial C}{\partial x} \right)^2 + \left(\frac{\partial C}{\partial y} \right)^2 + \left(\frac{\partial C}{\partial z} \right)^2 \right]. \tag{2.13}$$

While this is sufficient for laminar cases, modifications must be made to Equation 2.13 for the turbulent flow regime. Kock and Herwig have shown that the effect of turbulence in the k-ε model can be added to the above formula by adding a value of the pseudo-dissipation or indirect dissipation [39], found by the equation

$$\dot{S}_{D'} = \frac{\rho \epsilon}{T}. \tag{2.14}$$

Thus, we can account for both the entropy production rate by direct viscous dissipation, $\dot{S}_F'''$, and the entropy production rate by indirect (ie: turbulent) dissipation.

Einstein showed that the diffusion coefficient could be found from the mean-square displacements of particles within a fluid. It relies on a condition of dynamic equilibrium between opposing forces being established within the fluid, and does not depend upon which forces are involved in the setup of that equilibrium [23]. The equation arose from considering the Brownian motion of particles under an osmotic pressure, though applies to many other situations.

$$D = \frac{RT}{N} \cdot \frac{1}{6\pi\mu r} = \frac{k_B T}{6\pi\mu r}. \tag{2.15}$$

The diffusion coefficient used in these equations was extracted from lists of self-diffusion coefficients for water [40]. While self-diffusion coefficients can be calculated using the formula

$$D_i^* = D_i \frac{\partial(\ln C_i)}{\partial(\ln a_i)}. \tag{2.16}$$

where a_i is the activity coefficient of species i in the solution [41].

Chapter 3: Numerical Methods

This chapter will list and describe the settings used within the computational fluid dynamics (CFD) modeling software that was used for this thesis. Ansys® Fluent®, a module of Ansys Workbench™ 16.1, was the CFD software used for this study. The model geometry was originally created with SOLIDWORKS® 2015 and meshed with Workbench's built in meshing tool, which is simply called Ansys Meshing™.

3.1: Fluent Settings

The models enabled for these simulations were the Laminar Viscosity model and the Species Transport Species model. Enabling these models also automatically enables the Energy model though testing indicated that the results of this model did not alter simulation outcomes, and so it was manually disabled to save computation time on each simulation.

Several flows did not converge and after some trials were found to be turbulent. In these cases, the Turbulent k-ϵ model was enabled.

3.2: Fluent Processing

All sorts of flows within Fluent solve the conservation equations for both mass and momentum. As this particular set of simulations also deal with species transport, the solver also calculates the conservation for each species involved.

Equations in this chapter all use the nomenclature of Fluent's Theory Guide [42] rather than the nomenclature otherwise established for this document.

The conservation equation for mass is identical to that which was presented in the previous chapter. The form of the conservation of momentum equation is somewhat different [42]. It uses the following equation to calculate the conservation of momentum:

$$\frac{\partial \rho \mathbf{v}}{\partial t} + \nabla \cdot (\rho \mathbf{v} \mathbf{v}) = -\nabla p + \nabla \cdot (\bar{\bar{\tau}}) + \rho \mathbf{g} + \mathbf{F}. \tag{3.1}$$

In this case the $\bar{\bar{\tau}}$ is the stress tensor, which will be described next. The last two terms are for the gravitational body force and external body forces, respectively. The stress tensor is described by:

$$\bar{\bar{\tau}} = \mu \left[(\nabla v + \nabla v^{\mathrm{T}}) - \frac{2}{3} \nabla \cdot v I \right], \tag{3.2}$$

where I is the unit tensor and the second term on the right hand side is the effect of volume dilation.

When calculating the conservation of different fluid species, Fluent uses the following convection-diffusion equation to predict the mass fraction of each species Y_i:

$$\frac{\partial}{\partial t} (\rho Y_i) + \nabla \cdot (\rho \mathbf{v} Y_i) = -\nabla \cdot \mathbf{J}_i + R_i + S_i, \tag{3.3}$$

where R_i is the net rate of production by chemical reaction (0 for this simulation) and S_i is the rate of creation by addition from the dispersed phase plus user-defined sources (which is also 0). This equation is solved for N-1 species, where N is the number of fluid phase species in the system. Since this model uses two such species, this equation is solved once for each cell in the simulation.

The value $\mathbf{J}_i$ is the diffusion flux of the species. Fluent uses Fick's law to model mass diffusion due to concentration gradients, which can be written as:

$$J_i = -\rho D_{i,m} \nabla Y_i - D_{\mathrm{T},i} \frac{\nabla T}{T} \tag{3.4}$$

where $D_{i,m}$ is the mass diffusion coefficient and $D_{\mathrm{T},i}$ is the thermal diffusion coefficient.

Turbulent flow mass diffusion is modeled differently, however, and uses the following formula to obtain the diffusion flux:

$$J_i = -\left(\rho D_{i,m} + \frac{\mu_t}{Sc_t}\right) \nabla Y_i - D_{\mathrm{T},i} \frac{\nabla T}{T} \tag{3.5}$$

where Sc_t is the turbulent Schmidt number. This defaults to a value of 0.7, but can be expressed as

$$Sc_t = \frac{\mu_t}{\rho D_t} \tag{3.6}$$

where μ_t is the turbulent viscosity and D_t is the turbulent diffusivity.

Fluent's implementation of the k-ϵ model for turbulent flows uses the following two equations for the transport of k, the turbulent kinetic energy, and ϵ, the rate of turbulent dissipation:

$$\frac{\partial}{\partial t}(\rho k) + \frac{\partial}{\partial x_i}(\rho k u_i) = \frac{\partial}{\partial x_j}\left[\left(\mu + \frac{\mu_t}{\sigma_k}\right)\frac{\partial k}{\partial x_j}\right] + G_k + G_b - \rho\epsilon - Y_M + S_k \tag{3.7}$$

and

$$\frac{\partial}{\partial t}(\rho\epsilon) + \frac{\partial}{\partial x_i}(\rho\epsilon u_i) = \frac{\partial}{\partial x_j}\left[\left(\mu + \frac{\mu_t}{\sigma_\epsilon}\right)\frac{\partial\epsilon}{\partial x_j}\right] + C_{1\epsilon}\frac{\epsilon}{k}(G_k + C_{3\epsilon}G_b) - C_{2\epsilon}\rho\frac{\epsilon^2}{k} + S_\epsilon. \tag{3.8}$$

G_k is the generation of turbulent kinetic energy due to mean velocity gradients,

$$G_k = -\rho \overline{u_i' u_j'} \frac{\partial u_j}{\partial x_i}. \tag{3.9}$$

G_b is the generation of turbulent kinetic energy due to buoyancy,

$$G_b = \beta g_i \frac{\mu_t}{\mathrm{Pr}_t} \frac{\partial T}{\partial x_i}, \tag{3.10}$$

where Pr_t is the turbulent Prandtl number for energy and g_i is the component of the gravitational vector in the ith direction. For this model the default value of Pr_t is 0.85 in the standard and realizable k-ϵ models. The coefficient of thermal expansion, β, is defined as

$$\beta = -\frac{1}{\rho}\left(\frac{\partial \rho}{\partial T}\right)_p. \tag{3.11}$$

Y_M is the contribution of fluctuating dilation in compressible turbulence to the overall dissipation rate,

$$Y_M = 2\rho\epsilon M_t^2, \tag{3.12}$$

where M_t is the turbulent Mach number, defined as

$$M_t = \sqrt{\frac{k}{a^2}}, \tag{3.13}$$

where $a \equiv \sqrt{\gamma R T}$ is the speed of sound.

S_k and S_ϵ are user-defined source terms. The turbulent viscosity μ_t is computed with a combination of k and ϵ:

$$\mu_t = \rho C_\mu \frac{k^2}{\epsilon}. \tag{3.14}$$

13

$C_{1\epsilon}$, $C_{2\epsilon}$, and C_μ are constants and σ_k and σ_ϵ are the turbulent Prandtl numbers for k and ϵ

respectively – their values are all provided in the previous chapter, but are repeated here:

$$C_\mu = 0.09 \quad C_1 = 1.44 \quad C_2 = 1.92 \quad \sigma_K = 1.0 \quad \sigma_\epsilon = 1.3.$$

$C_{3\epsilon}$ moderates how much ϵ is affected by buoyancy. It is calculated with the following relation:

$$C_{3\epsilon} = \tanh \left| \frac{v}{u} \right|. \tag{3.15}$$

Fluent discretizes these equations using the finite volume method. These equations are then

solved for each control volume and solved numerically. These transport equations can be

generalized as transporting the generic scalar quantity ϕ. The equation is integrated over the

control volume V:

$$\int_V \frac{\partial \rho \phi}{\partial t} dV + \oint \rho \phi u d\mathbf{A} = \oint D_\phi \nabla \phi \cdot d\mathbf{A} + \int_V S_\phi dV, \tag{3.16}$$

where $\mathbf{A}$ is the surface area vector and D_ϕ is the diffusion coefficient for the quantity ϕ and S_ϕ is

the source of ϕ per unit volume. This equation is discretized for a given cell as

$$\frac{\partial \rho \phi}{\partial t} V + \sum_f^{N_{faces}} \rho_f \mathbf{u}_f \phi_f \cdot \mathbf{A}_f = \sum_f^{N_{faces}} D_f \nabla \phi_f + S_\phi V, \tag{3.17}$$

where N_{faces} is the number of faces enclosing a cell, ϕ_f is the value of the quantity ϕ convected

through face f. The quantity $\rho_f \mathbf{u}_f \phi_f \cdot \mathbf{A}_f$ is the mass flux through the face.

Fluent provides several options for solution methods for pressure-velocity coupling and for

spatial discretization. For all simulations, this work utilized the SIMPLE scheme for pressure-

velocity coupling. The SIMPLE algorithm enforces mass conservation by using the relationship between velocity and pressure corrections.

$$a_P p' = \sum_{nb} a_{nb} p'_{nb} + \sum_{f}^{N_{faces}} J_f^* A_f \qquad (3.18)$$

where p' is the pressure correction.

There are different solution methods available for (in this simulation) four different spatial discretization options. For the Gradient setting, the Least Squares Cell-Based option was selected. For the Pressure setting, the Second Order method was used. For both the Momentum and h2o<l> (one of the species being transported) settings, the Second Order Upwind option was used.
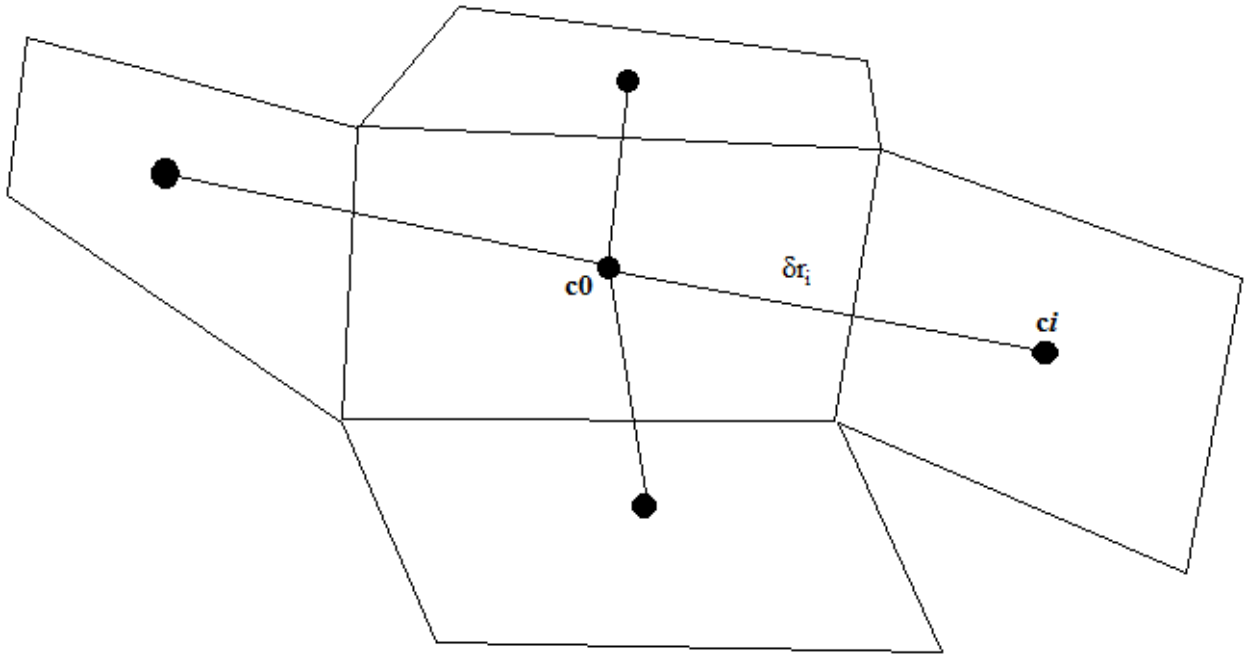

Figure 2: Cell Centroid Evaluation

The Least Squares Cell-Based Gradient Evaluation estimates the gradient between cells to be the difference between centroids of the cells along the vector connecting those centers,

$$[J](\nabla\phi)_{c0} = \Delta\phi,$$ (3.19)

where $[J]$ is the coefficient matrix where it a function of geometry and $c0$ represents a central cell from which we are trying to find gradients to cells ci (see Figure 2).

The Second-Order Upwind Scheme computes quantities at cell faces using a multidimensional linear reconstruction approach [43]. Using a Taylor series expansion of cell-centered solutions about the cell centroid, this approach achieves a higher-order accuracy at the cell faces.

The pressure solver, set to the Second-Order scheme, reconstructs the face pressure in the manner described above for convection terms. This method can have trouble with bad meshes or in flows with discontinuous pressure gradients, but these issues were not present in the simulations run for this thesis.

3.3: Post-Processing

Entropy generation was calculated in parts within VisIt, as each of these parts is summed to find the total volumetric entropy generation. The frictional or advective part of the entropy generation was calculated using Equation 2.8, reprinted here:

$$\dot{S}_F''' = \frac{\mu}{T_o}\left[2\left(\left(\frac{\partial u}{\partial x}\right)^2 + \left(\frac{\partial v}{\partial y}\right)^2 + \left(\frac{\partial w}{\partial z}\right)^2 + \left(\frac{\partial u}{\partial y} + \frac{\partial v}{\partial x}\right)^2 + \left(\frac{\partial u}{\partial z} + \frac{\partial w}{\partial x}\right)^2 + \left(\frac{\partial v}{\partial z} + \frac{\partial w}{\partial y}\right)^2\right)\right],$$ (2.8)

where T_o is set to 300K, and values for viscosity and the partial derivatives were extracted from the CGNS file.

The diffusive part of the equation was calculated using Equation 2.11, reprinted here:

$$\dot{S}_D''' = \frac{RD}{C_o}\left[\left(\frac{\partial C}{\partial x}\right)^2 + \left(\frac{\partial C}{\partial y}\right)^2 + \left(\frac{\partial C}{\partial z}\right)^2\right],$$ (2.11)

with a R=8.3145, D=2x10^{-7} and C_o picked based on the flow ratio according to Table 1, below. The CGNS files did not have values for concentrations along each dimension assigned to individual variables. Instead, it contains an data object called "`Mass_fraction_of_h2o_l_`", which is a vector that contains these values for the entire model. Thus, the equation within VisIt, which requires the gradient of a scalar quantity, C, contains three parts similar to "`gradient(Mass_fraction_of_h2o_l_)[0]`", with the index [0] representing values for the x-axis, the index [1] representing the y-axis, and the index [2] representing the z-axis. In this case the square braces, [], are VisIt's vector component operator, which is able to construct a lower-rank tensor from a higher rank tensor – in this case, it creates a scalar from a vector [44].

The value C_o is a product of the flow weightings and is different for each of the inlet flow ratios. The values used are represented in Table 1.

Table 1: C0 values for Flow Ratios

Flow Ratio	C_o
1:1	0.50000000
1:2	0.33333333
1:5	0.16666666
1:10	0.09090909

For the turbulent cases, an additional turbulent term had to be calculated. This was derived from Equation 2.14, replicated here:

$$S_{PRO,D'} = \frac{\rho \varepsilon}{T}, \tag{2.14}$$

where T=300K, $\rho = 998.2$ and ε was extracted from the CGNS file.

The total volumetric entropy generation was thus the sum of Equations 2.8, 2.11, and (for turbulent cases only) 2.14.

Chapter 4: Methodology

As mentioned in the previous chapter, the model geometry was created using SOLIDWORKS 2015. It was then exported as a parasolid file and loaded into Ansys Workbench 16.1. The model was tagged in Ansys DesignModeler™ and then meshed using Ansys Meshing. Simulations were carried out with Fluent, with selected result values exported in CGNS file format and then post-processed with VisIt.

4.1: The Buddy Supercomputer Cluster

All of the geometry modelling, simulations, and some of the post-processing were accomplished with (and, indeed, would have been impossible without) the Buddy Supercomputer Cluster at the University of Central Oklahoma. Buddy is a 37-node Linux cluster with 31 compute nodes (each with 20 CPUs and 64GB of memory), 4 high-memory compute nodes (with 128GB of memory), and 2 GPU nodes. Simulations typically utilized 55-60 processors (a limit imposed by available Fluent licenses) on 3-6 compute nodes. Laminar simulations were conducted between October 24-27, 2019, while turbulent simulations ran from December 12-18 of the same year. See Appendix 1 for file naming conventions and example scripts.

4.2: Model Specifications

The model itself consists of two inlets that flow together into a series of square-shaped obstacles that split apart and recombine the flow. The last quarter of the model is dedicated to a straight section to allow flow to develop before reaching the outflow. The model, despite appearances, is asymmetrical. Each of the 'neck' sections between the larger 'square' sections is slightly offset from center, and alternate which direction they're offset. The model was created on the meter

scale in SOLIDWORKS and was scaled by a factor of 0.001 in Ansys DesignModeler when the

geometry was imported for tagging and meshing.
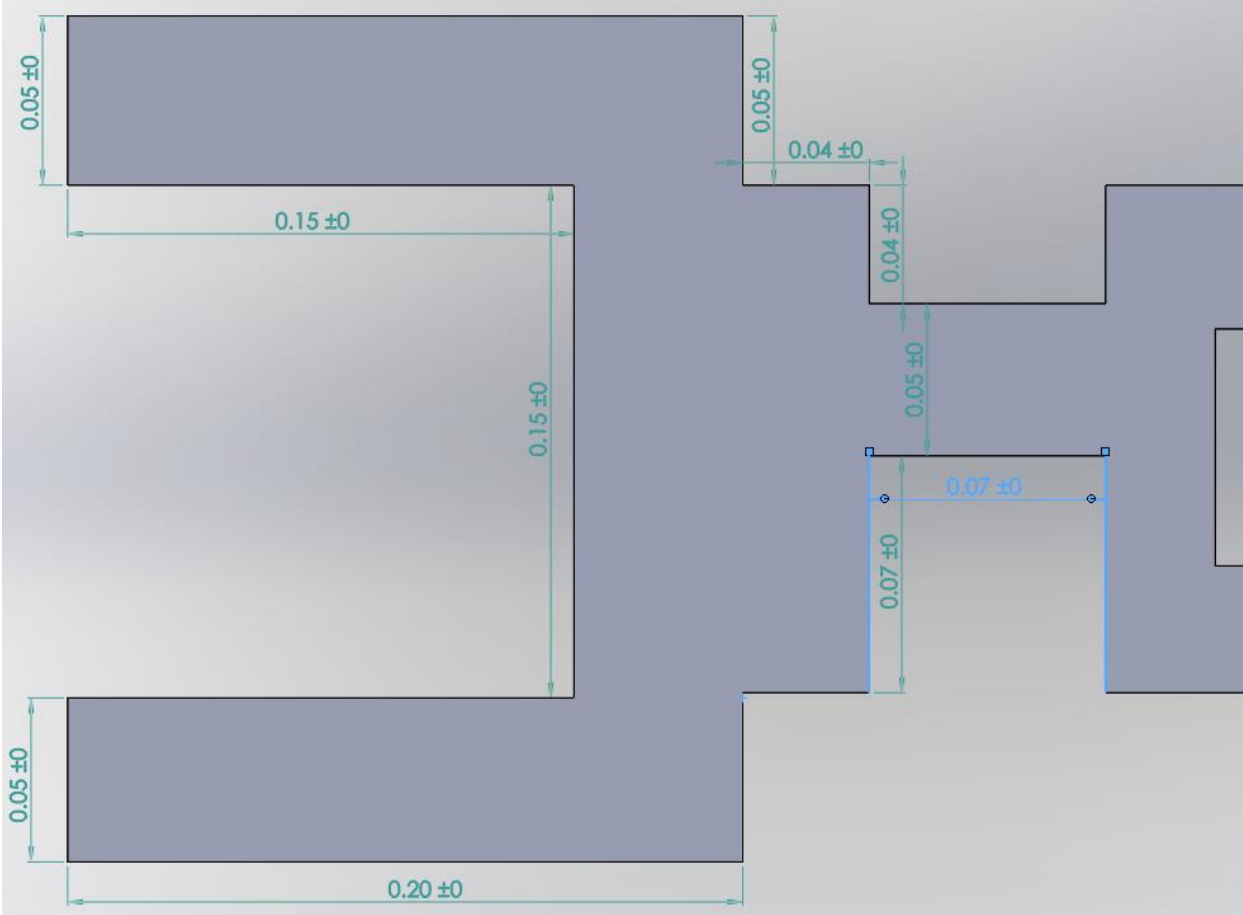

Figure 3: Model Dimensions Near Inlets
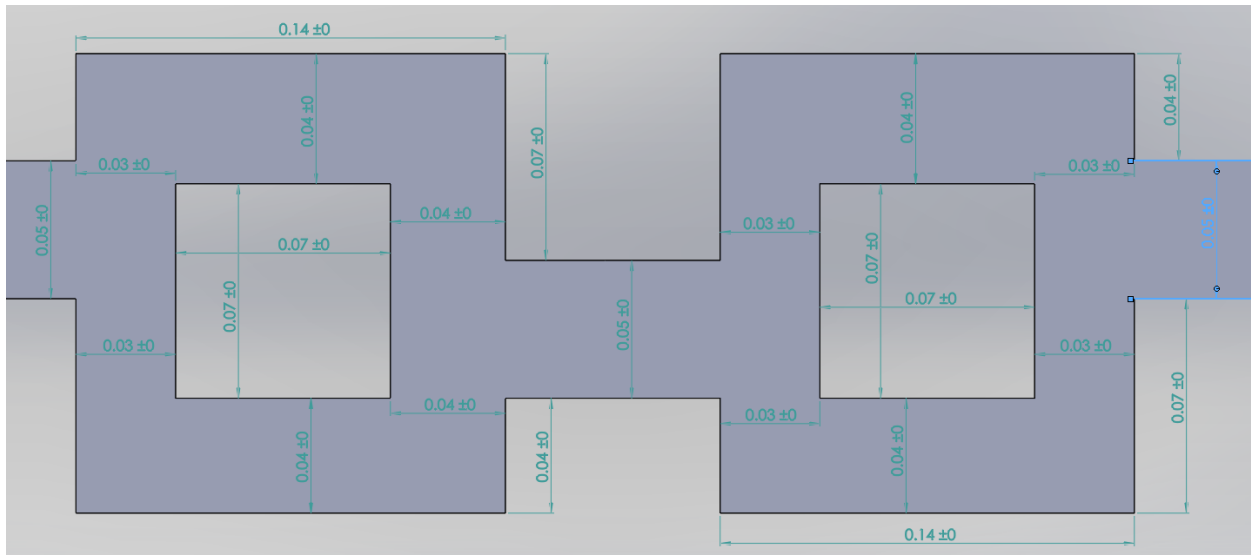
Figure 4: Model Dimensions in Main Body
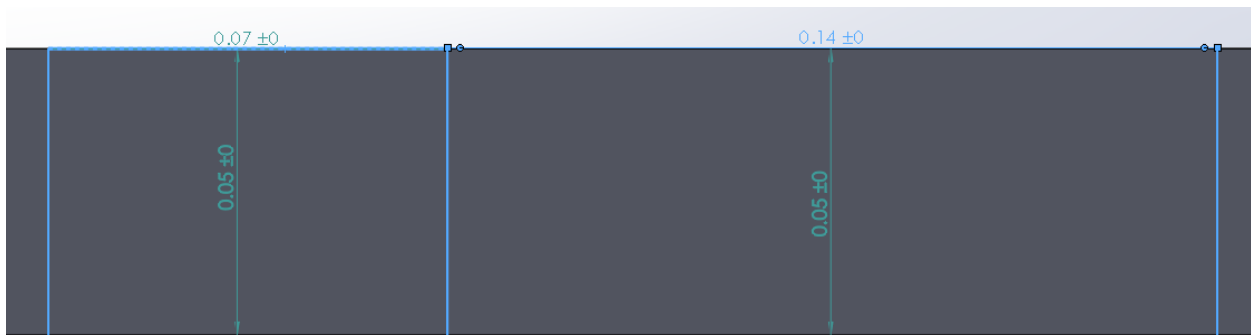
Figure 5: Model Dimension Depth
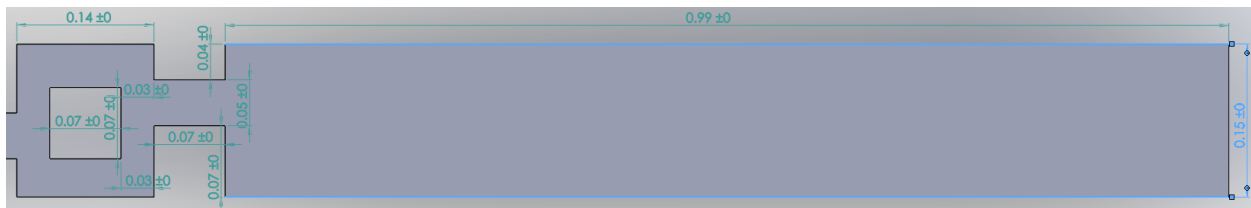
Figure 6: Model Dimensions Near Outflow

4.3: VisIt Value Testing

VisIt's output options were not very clear, so a small slab was modeled and meshed. Values for

entropy generation within this model were calculated by Dr. Evan Lemley, and these values were

compared this with various output options within VisIt to determine that the value for entropy generation we were interested in was labeled the Weighted Variable Sum [45].

Figure 7: Value Testing Model

4.4: Validity of Disabling the Energy Solver

Two simulations were carried out with identical conditions with the exception that one included the energy solver and one did not. The variance was sampled at 15 points on both simulations and the mixing index was calculated. The graph of those samples is below.
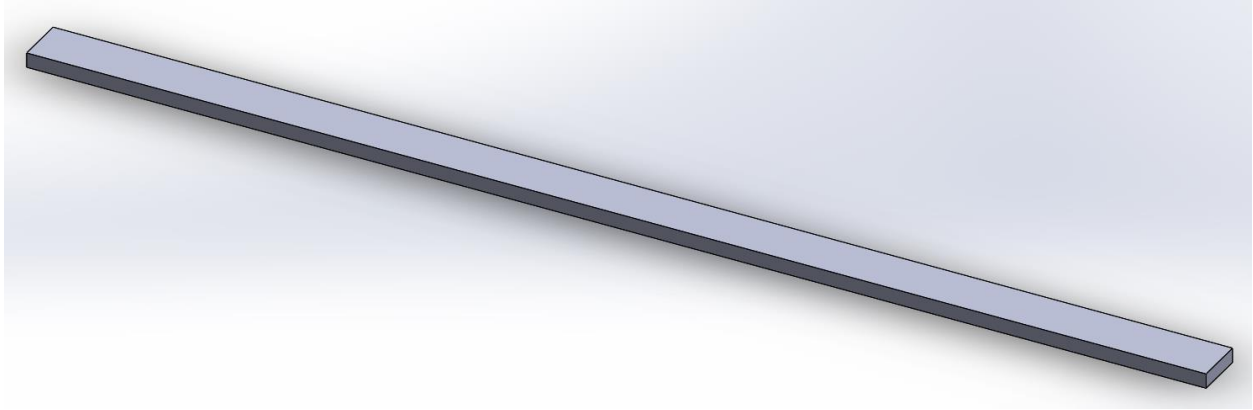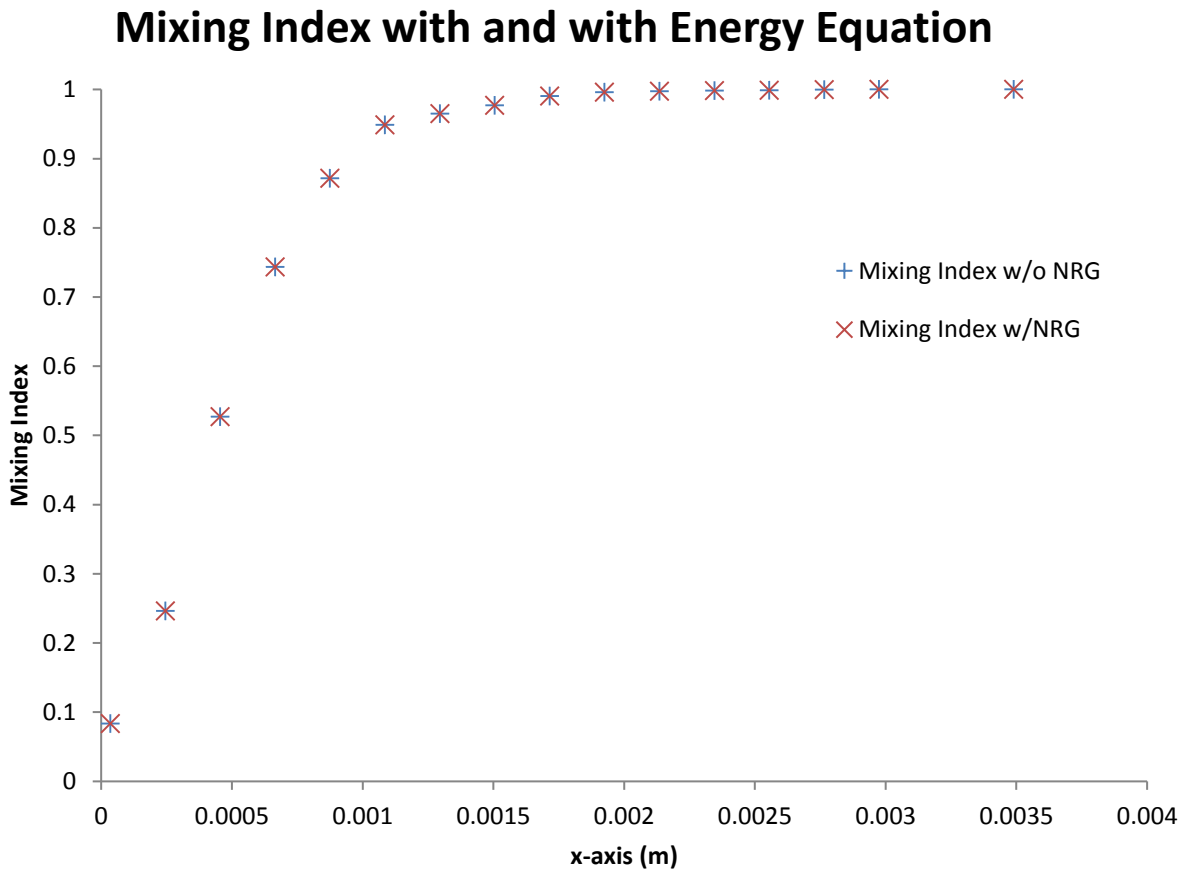

Figure 8: Mixing Index Values with and without the Energy Equation Solver

The largest percent difference between any pair of values was 5.6×10^{-6}, and most differences were smaller than that by two or more orders of magnitude. The entropy generation was also determined for both models and found to have a percent difference of 9.8×10^{-6}. As a result, it was determined that disabling the energy solver would result in substantially the same values and would save considerable computation time. The energy solver was disabled in all subsequent simulations. See Appendix X for the table of values and percent differences.

4.5: Mesh Analysis

Meshing within Ansys Meshing was controlled by setting minimum and maximum edge size without enforcing any particular element shape. This resulted in a hexahedral mesh with mostly-cube-shaped elements that tended to get distorted toward the junctions where flow would split or recombine.
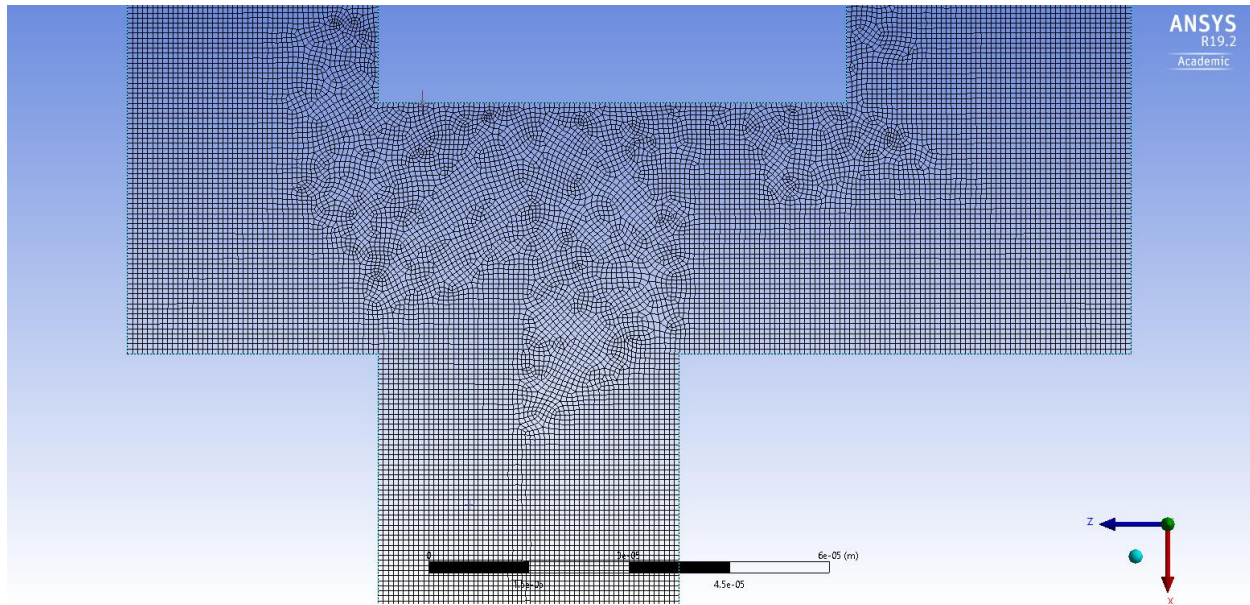
Figure 9: Mesh Detail

In order to ensure that experimental simulations were not dependent on mesh densities, five different meshes using the model were created and tested using fluid velocities corresponding to Re 1 and Re 50 at each inlet. Values for entropy generation and mixing index were examined for these ten cases. Values appeared to be largely constant across all meshes, and so a determination was made to use the 4.6 million node mesh, the second smallest, in order to accelerate computation times by keeping the number of nodes smaller. See Appendix 3 for tables related to the mesh analysis.

Figure 10: Mesh Analysis Graphs

4.6: Simulation Set-Up

During the analysis of the data, it is often useful to simply refer to cases in terms of their overall Reynolds number. This Total Reynolds Number, Re_T, is the sum of the Reynolds numbers of the two inlets. That is

$$Re_T = Re_{inlet\ 1} + Re_{inlet\ 2}. \tag{4.1}$$

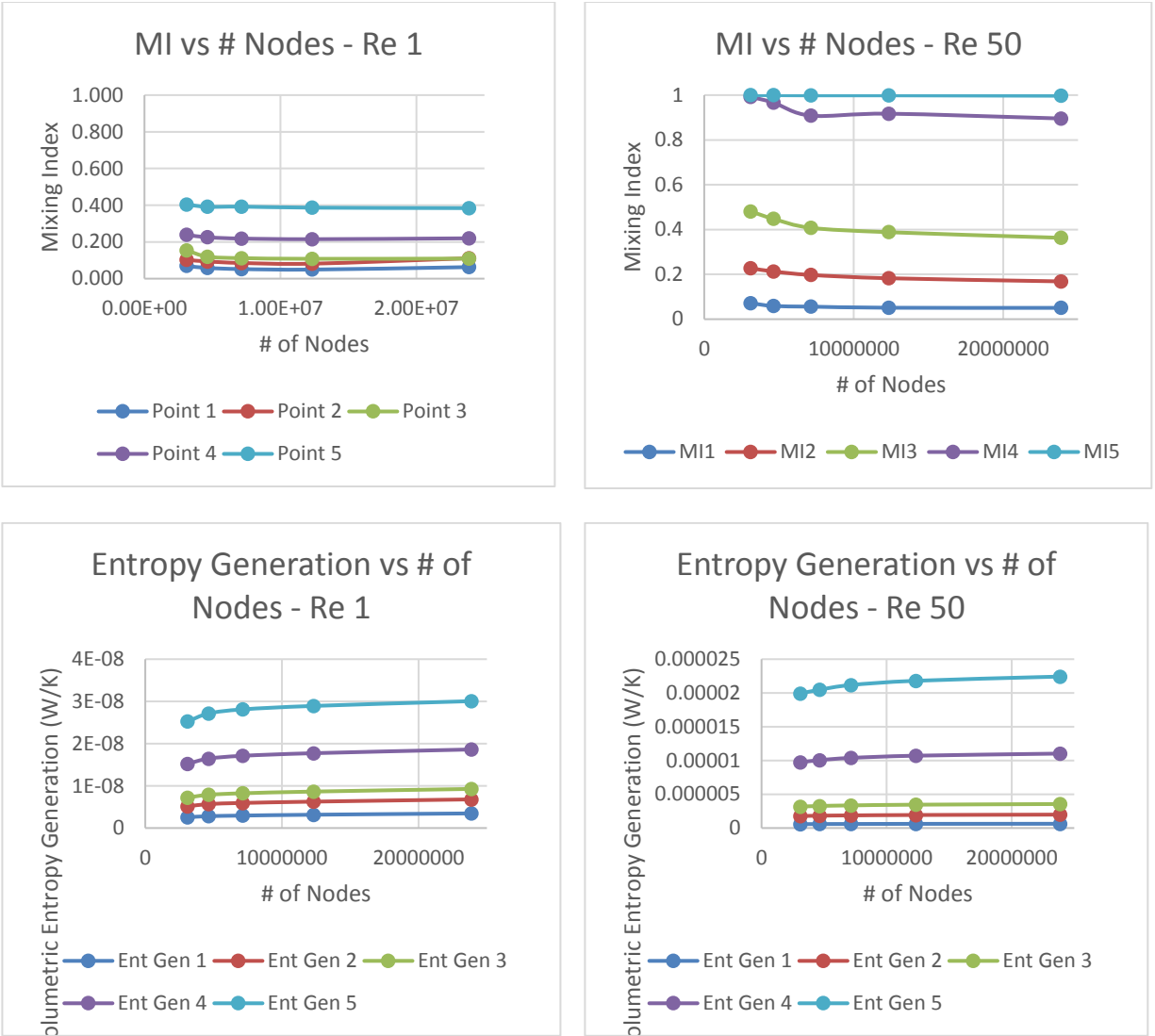As one of the investigations included in this thesis includes an analysis of the effects of the ratio of inlet flow ratios, deciding what these ratios would be was key to setting up the simulations themselves. The 1:1 flow ratio seems an obvious choice, as it provides the baseline of comparison for all other ratios. Three other ratios were also selected: 1:2, 1:5, and 1:10. In the end, there were 26 laminar simulations and an additional 12 turbulent cases. Each case is named according to the Reynolds number (Re) at the two inlets for that case. For Re<1, leading zeros, including the one before the decimal, were retained in these names to help differentiate the cases. For the single case with a decimal in the middle of the selected Reynolds number, the letter 'd' was substituted in order to not interrupt the file name with possible interpretations of a file-type suffix. For the 1:1 cases, the cases were simply named things like Re1, Re05, or Re10, as both inlets have the same Re value. Other cases have names like Re005Re01 (for the 1:2 case with inlets of Re 0.05 and Re 0.1), Re1Re5 (for the 1:5 case with inlets Re 1 and Re 5), and Re10Re100 (for the 1:10 case with inlet values of Re 10 and Re 100). Turbulent case names continue this trend and, in general, were all cases where Re_T was 150 or greater. They will be identified with a T suffixed to their case name to help differentiate them from laminar cases (ie: the case with a 1:5 ratio with Re 50 and Re 250 would be named Re50Re250T).

Tables 2 through 5 feature all of the simulated cases, their inlet Re values, and their total Re value.

Table 2: Case Parameters for Ratio 1:1

Ratio 1:1			
Case	Re_1	Re_2	Re_T
Re005	0.05	0.05	0.1
Re01	0.1	0.1	0.2
Re05	0.5	0.5	1
Re1	1	1	2
Re5	5	5	10
Re10	10	10	20
Re50	50	50	100
Re100T	100	100	200
Re200T	200	200	400
Re500T	500	500	1000

Table 3: Case Parameters for Ratio 1:2

Ratio 1:2			
Case	Re_1	Re_2	Re_T
Re005Re01	0.05	0.1	0.15
Re01Re02	0.1	0.2	0.3
Re05Re1	0.5	1	1.5
Re1Re2	1	2	3
Re5Re10	5	10	15
Re10Re20	10	20	30
Re25Re50	25	50	75
Re50Re100T	50	100	150
Re100Re200T	100	200	300
Re250Re500T	250	500	750

Table 4: Case Parameters for Ratio 1:5

Ratio 1:5			
Case	**Re_1**	**Re_2**	**Re_T**
Re005Re025	0.05	0.25	0.3
Re01Re05	0.1	0.5	0.6
Re05Re2d5	0.5	2.5	3
Re1Re5	1	5	6
Re5Re25	5	25	30
Re10Re50	10	50	60
Re25Re125T	25	125	150
Re50Re250T	50	250	300
Re100Re500T	100	500	600

Table 5: Case Parameters for Ratio 1:10

Ratio 1:10			
Case	**Re_1**	**Re_2**	**Re_T**
Re005Re05	0.05	0.5	0.55
Re01Re1	0.1	1	1.1
Re05Re5	0.5	5	5.5
Re1Re10	1	10	11
Re5Re50	5	50	55
Re10Re100	10	100	110
Re25Re250T	25	250	275
Re50Re500T	50	500	550
Re100Re1000T	100	1000	1100

Table 6: Inlet Velocities for Selected Re

Inlet Velocity (m/s)	**Re**	**Inlet Velocity (m/s)**	**Re**	**Inlet Velocity (m/s)**	**Re**
2.2383E-3	0.05	1.1191E-1	2.5	5.5957	125
4.4766E-3	0.1	2.2383E-1	5	8.9531	200
8.9531E-3	0.2	4.4766E-1	10	1.1191E+1	250
1.1191E-2	0.25	8.9531E-1	20	2.2383E+1	500
2.2383E-2	0.5	1.1191	25	4.4766E+1	1000
4.4766E-2	1	2.2383	50		
8.9531E-2	2	4.4766	100		

4.7: Post-Processing

Processed values were sampled at a number of locations within the models. A choice made early in the modelling of the device off-set the zero-point of the geometry's x-axis to approximately the point where the flows first converge, and so the x-axis was non-dimensionalized. Several points of interest were then picked and numbered to ease the
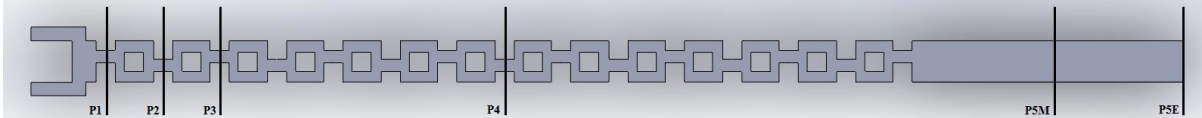

Figure 11: Selected Model Points

analysis.

Five points were picked to examine the Mixing Index and the Volumetric Entropy Generation. The number labels are largely the same, except for point 5, which was moved further inside the model due to edge effects. Point 5 for the Entropy Generation is at the outflow.

When applicable Point 5 will be referred to as Point 5M (for Mixing Index) or Point 5E (for Entropy Generation) to disambiguate which point is being referred to. All other points will simply be referred to as Point X (where X is the number of the point being referred to).

Points 1 through 4 were picked to be at the first three 'neck' sections and a neck section roughly in the middle of the mixer, while point 5 was picked to be toward the end of the model.

Chapter 5: Results

In examining the output data, a baseline is useful to compare the effects of varying the ratio of the inlet Reynolds numbers. After examining the case of ratio 1:1, the effects of varying the inlets can be examined in context. As the range of total Reynolds number, Re_T, and the range of values for volumetric entropy generation are both quite wide, many of the following graphs employ the use of logarithmic axes.

5.1: The 1:1 Ratio

5.1.1: Mixing Efficiency

The variance was sampled at five different points in each simulation and then Equation 2.7 was used to calculate a mixing index at each of those points. A few things become apparent after examining the data.
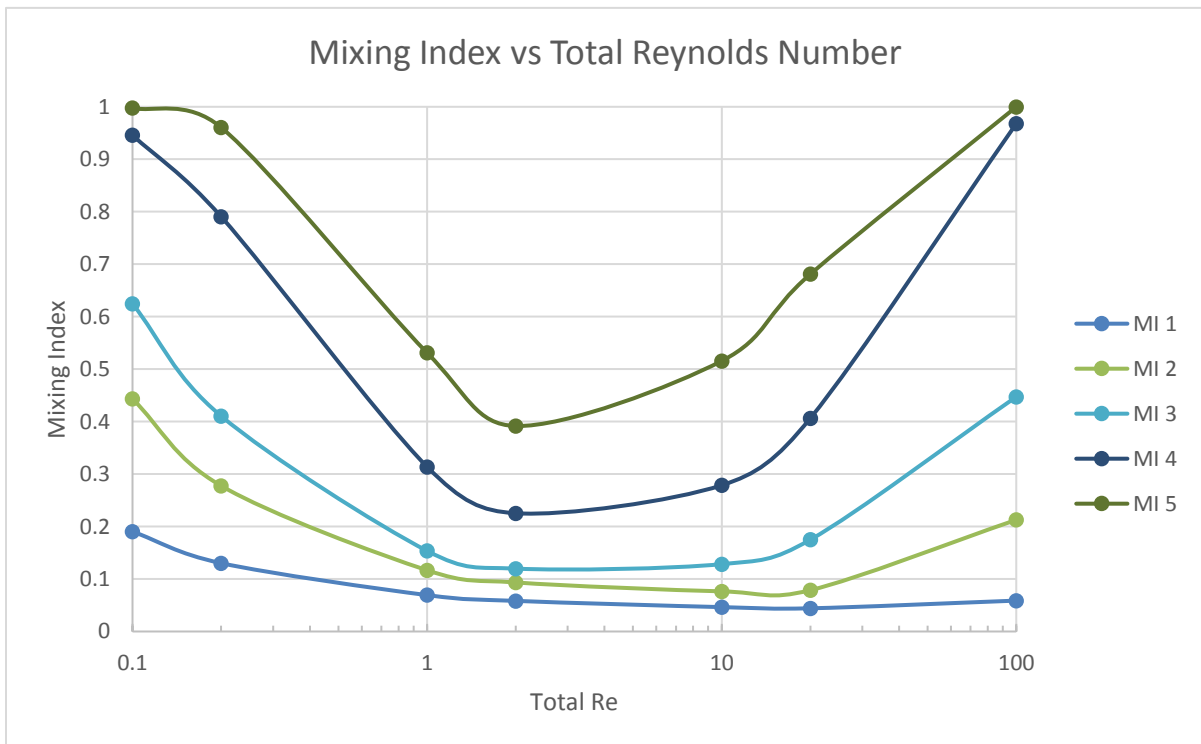

Figure 12: MI vs Total Re for 1:1 Ratio Cases

There are three different mixing regimes. For $Re_T<1$, mixing is good, but is poor between $Re_T=1$ and $Re_T=10$. As Re_T increases past 10, mixing continues to improve along with Re_T. Speculation suggests that mixing is good for very low Re_T due to extended residence time within the mixer, which can be confirmed by inspecting the entropy generation data (as is done in the next section). If that is the case, it is expected that diffusion will play a stronger role in entropy generation for low-Re flows. At $Re_T>10$, chaotic advection effects become prominent, and mixing improves as a result.
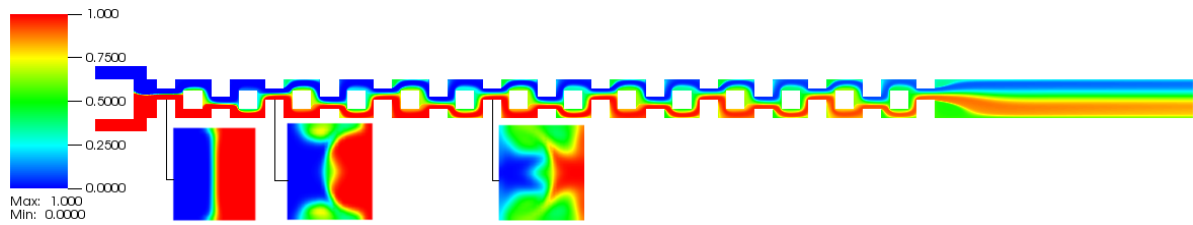

Figure 13: Mass Fractions in Midplane of Case Re10

An examination of vectors perpendicular to the overall flow, as in Figure 14, reveals that the obstacles are having the desired effect of inducing secondary flows conducive to mixing.
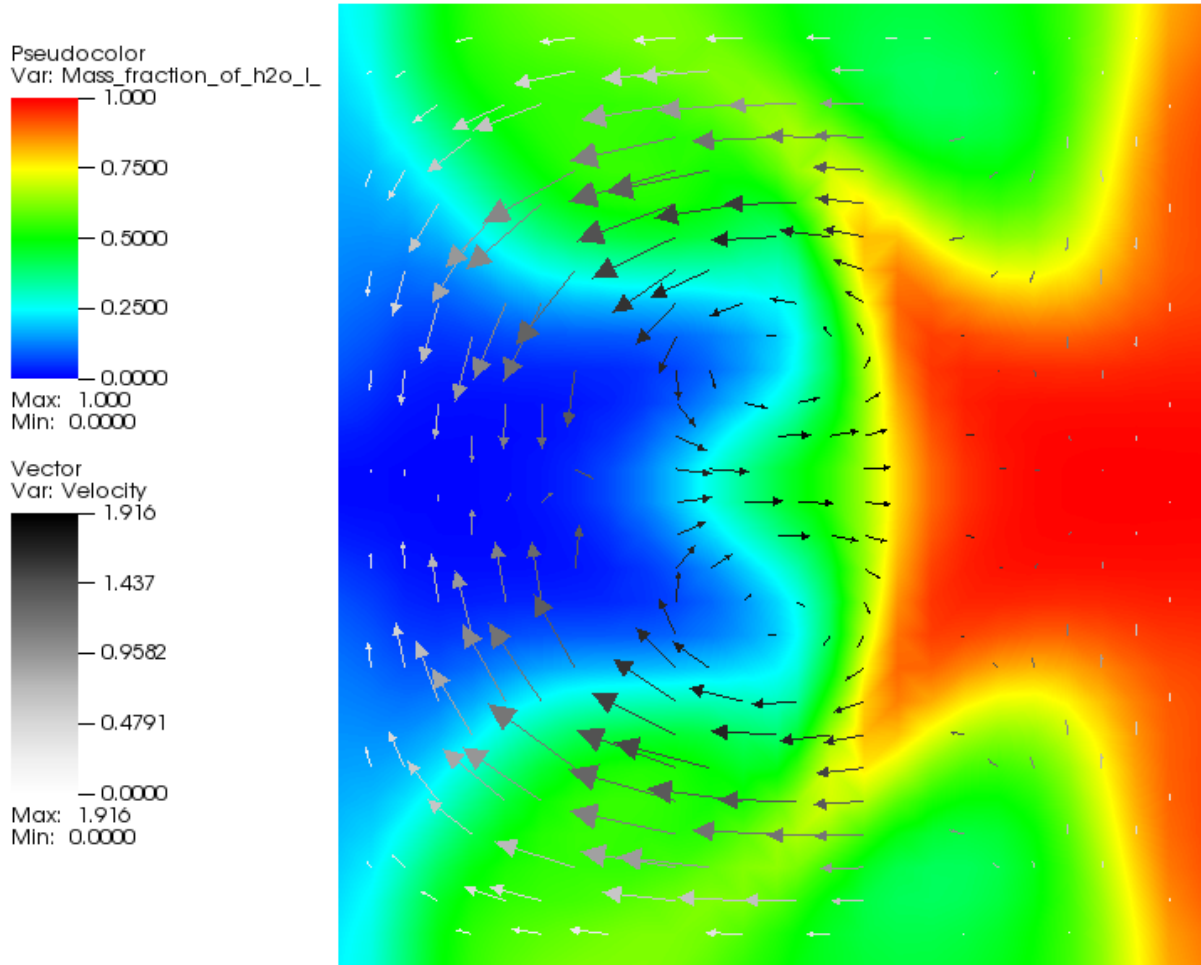
Figure 14: Mass Fractions in case Re10 at Point 4, with Velocity Vectors

5.1.2: Entropy Generation

Volumetric entropy generation values, $\dot{S}'''$, were sampled at 5 locations within the model for each simulation. Locations with larger values of $\dot{S}'''$ generally suggest features of the geometry that promote increased mixing [28]. It can be seen that the square obstacles and narrow constructions are having this effect, in Figures 15 and 16.

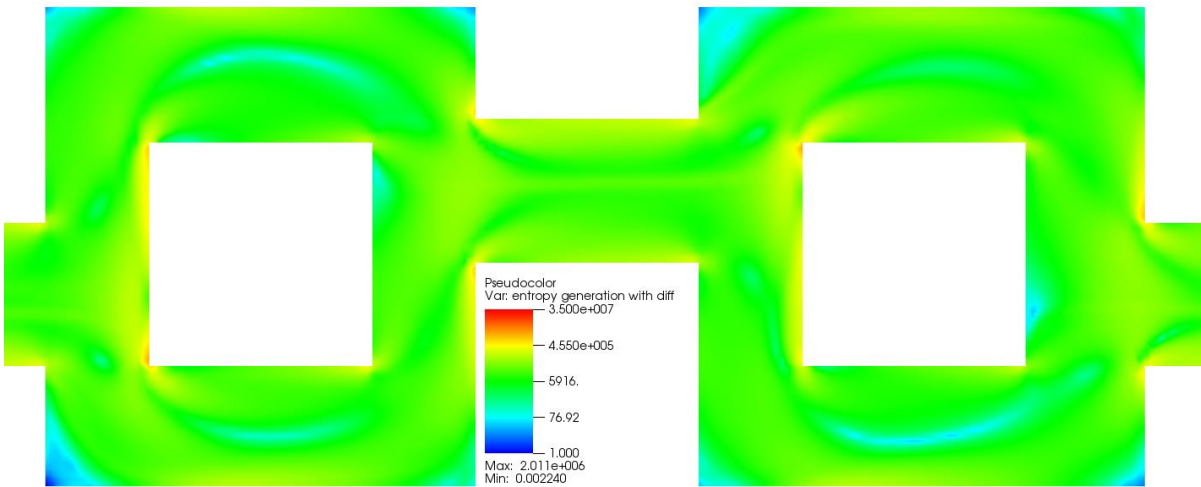Figure 15: Entropy Generation in the midplane of Case Re10

Figure 16: Entropy Generation in the midplane of Case Re10 - Detail Near Point 4
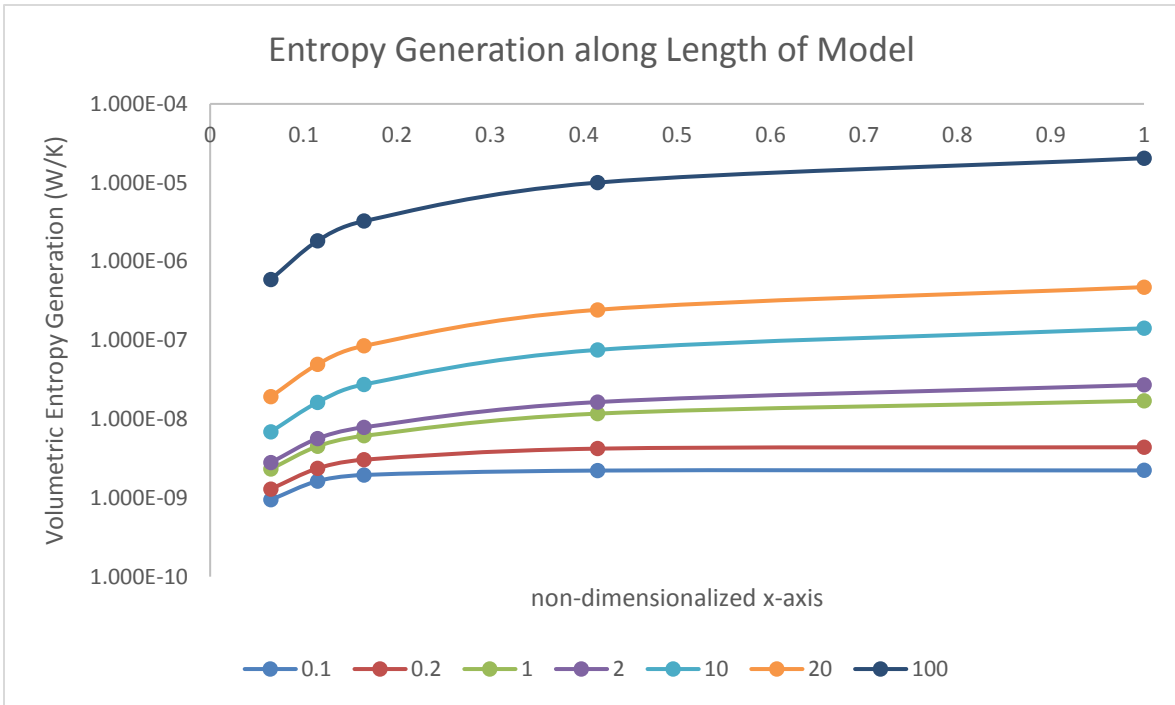
Figure 17: Entropy Generation along Length of Model

All entropy generation values increase along the length of the model in all cases, and so Point 4 was chosen to be a characteristic representation of entropy generation for each simulation. Additionally, because values for entropy generation from various sources was calculated separately, it is possible to examine the contributions from each individually, as seen in Figure 18.

Figure 18: Entropy Generation for a Typical 1:1 Case

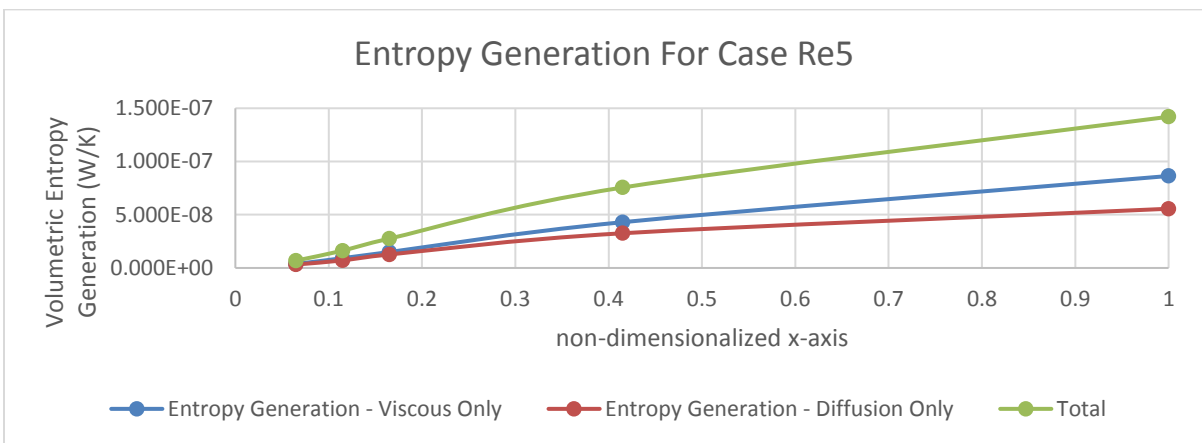From Figure 19, it is clear that diffusion plays a stronger role in lower-Re cases where residence time is longer. In the higher-Re cases, the contribution of diffusion becomes less and less relevant.
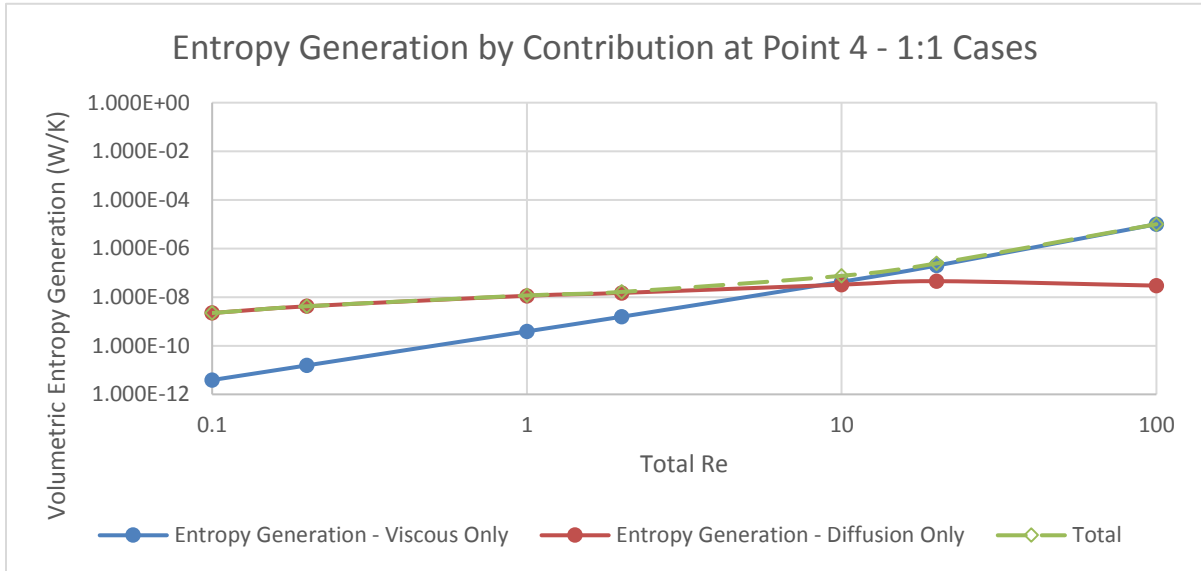
Figure 19: Breakdown of Viscous and Diffusive Contributions to Entropy Generation

5.2: Other Flow Ratios

With the 1:1 ratio baseline established, it can be compared to simulations with different flow ratios.

5.2.1: Mixing Index

The effects of different flow ratios on mixing efficiency appear at first glance to be significant, but it should be noted that less mixing has to occur in cases with higher flow ratios in order to achieve a fully-mixed state. That is, in the case of a 10:1 flow ratio, the

solution is already mostly composed of the solution being supplied at a higher rate.

Figure 20:Mixing Indices for All 1:2 Cases
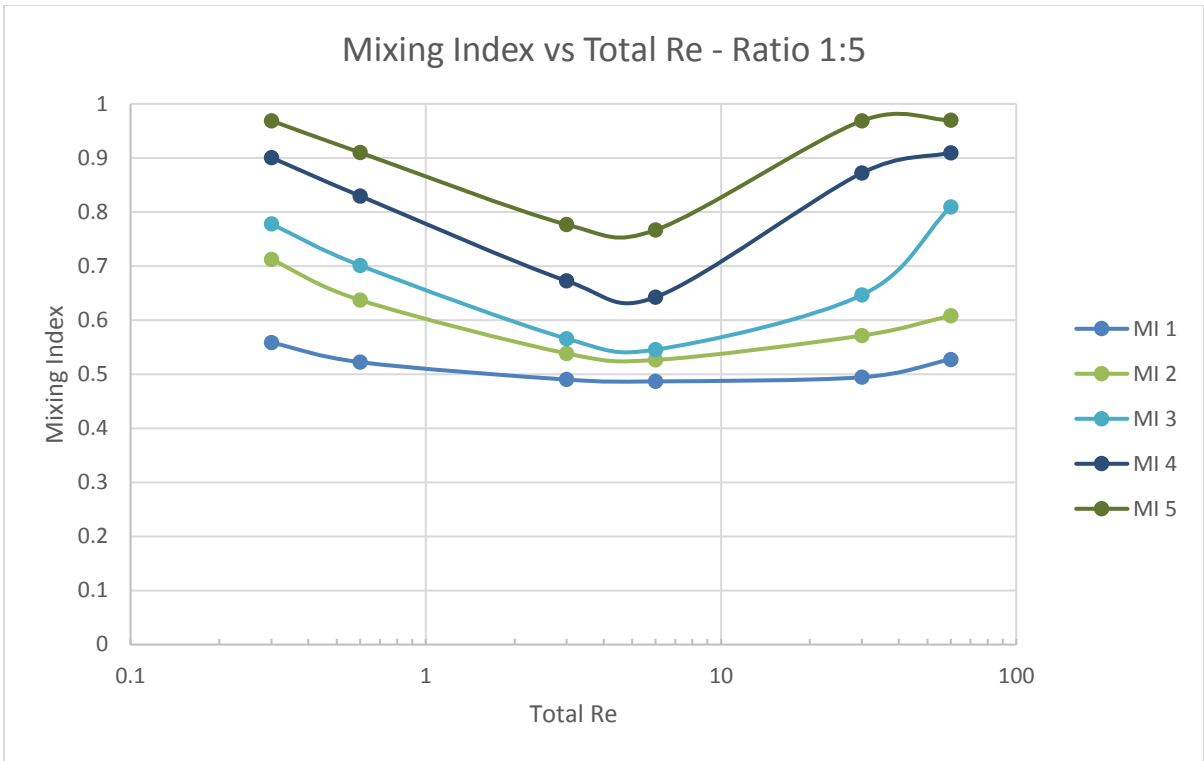
Figure 21: Mixing Indices for All 1:5 Cases
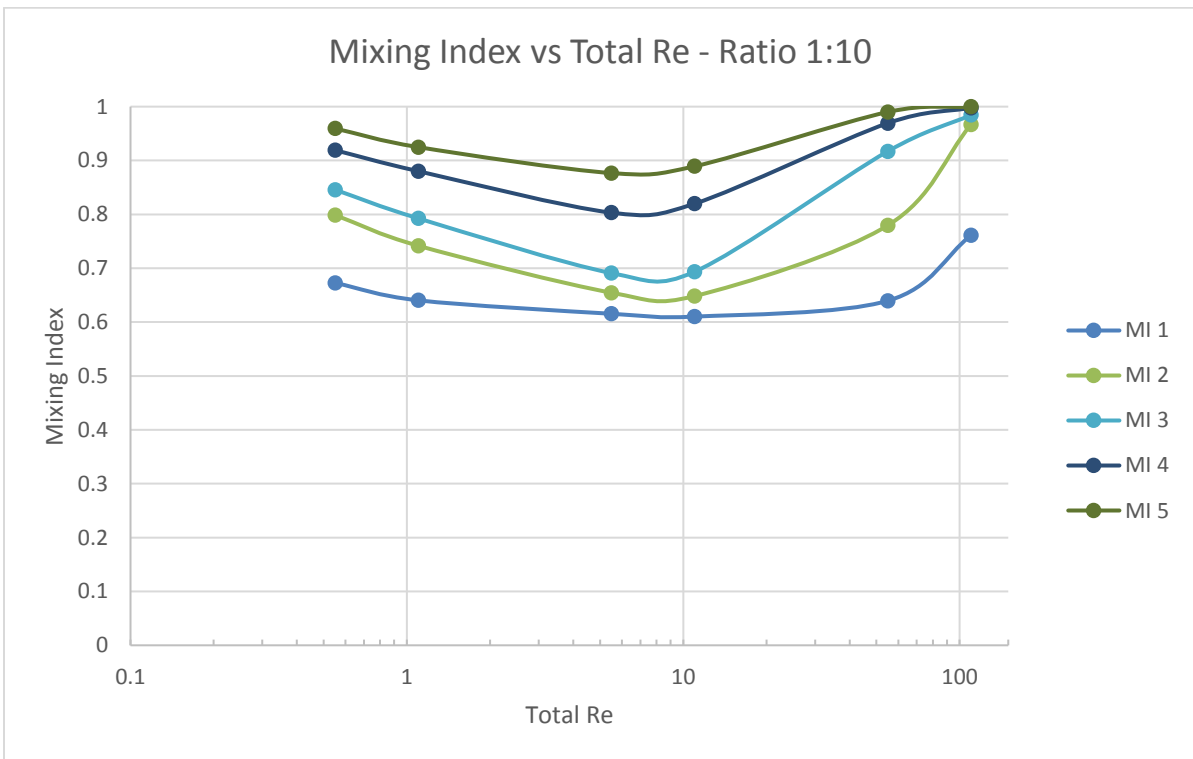
Figure 22: Mixing Indices for All 1:10 Cases

37

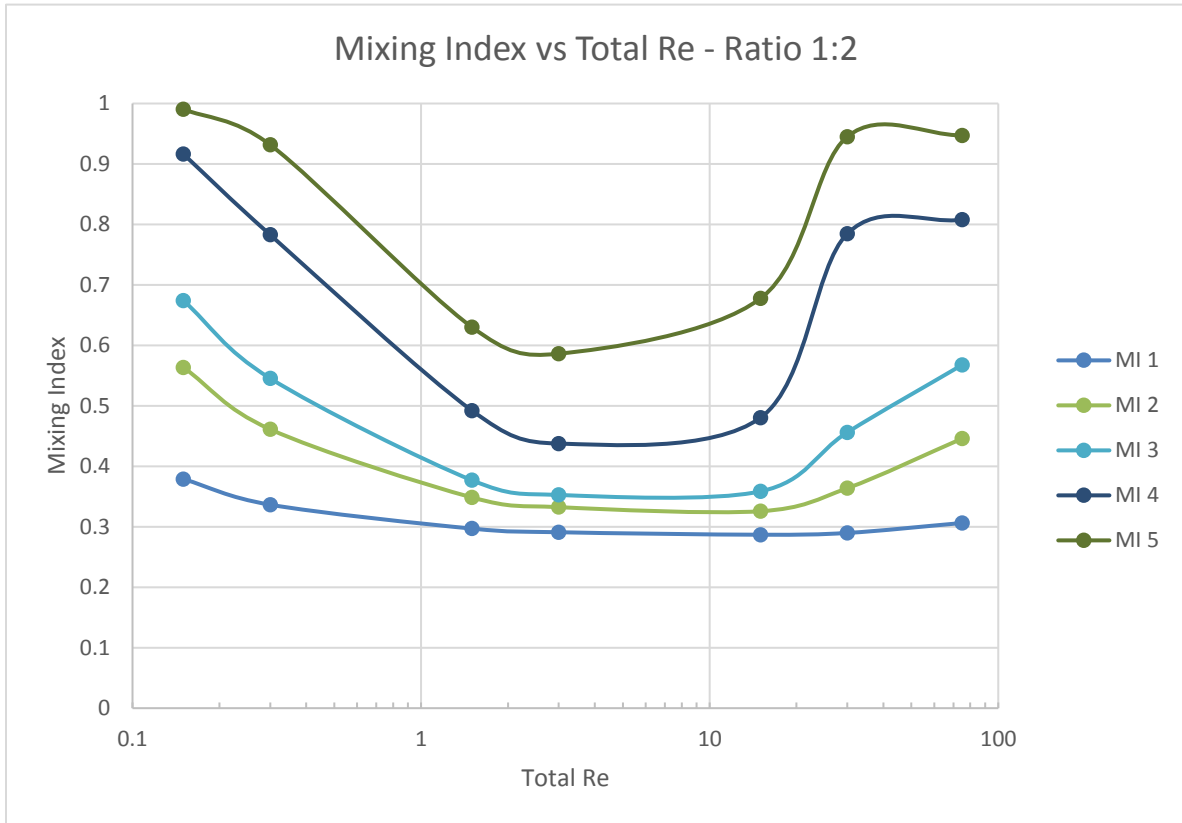It is clear from Figures 20-22 that the previous three regimes present for the 1:1 ratio are still evident here. Mixing in the range of $1 \leq Re_T \leq 10$ is significantly depressed. The 1:10 ratio cases also offer a first glimpse at a possible fourth regime for $Re_T > 100$. As it turns out, every simulation attempted for $Re_T > 110$ would not converge until turbulent models were enabled. Those cases will be explored in Section 5.4.
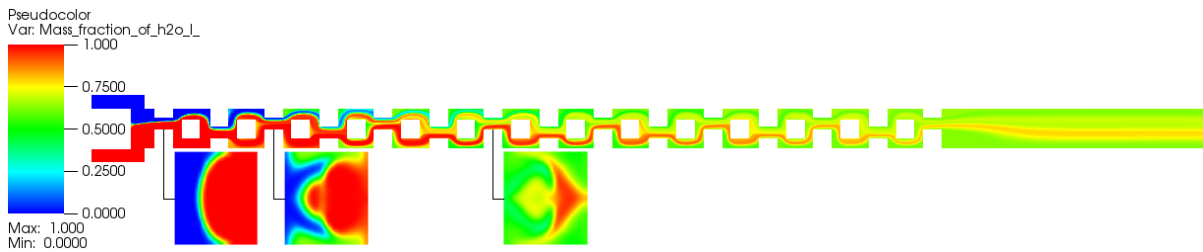
Figure 23: Mass Fractions in Midplane of Case Re10Re20
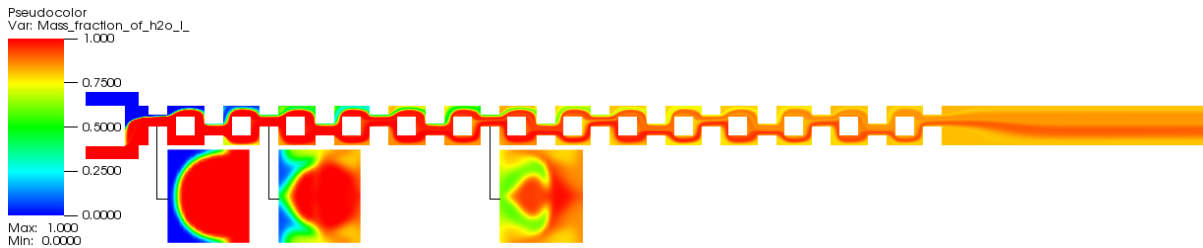
Figure 24: Mass Fractions in Midplane of Case Re5Re25
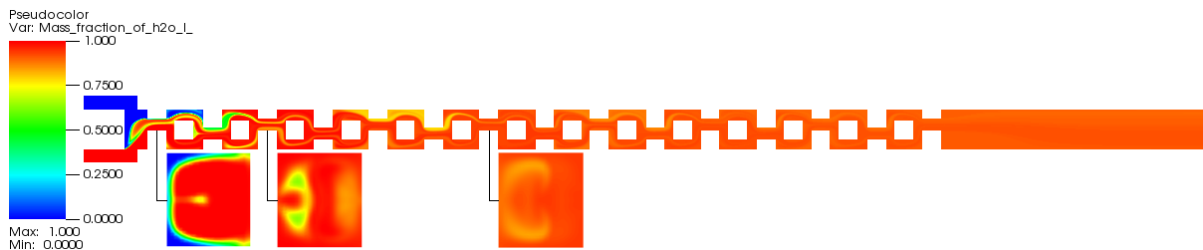
Figure 25: Mass Fractions in Midplane of Case Re5Re50

In breaking out mixing indices from Point 4, as in Figure 26, it is clear that superior mixing can be achieved by using $Re_T < 1$ or $Re_T > 10$; which of these is preferable depends on

application. It is also clear that a higher ratio of inlet flow rates increase the mixing effectiveness.
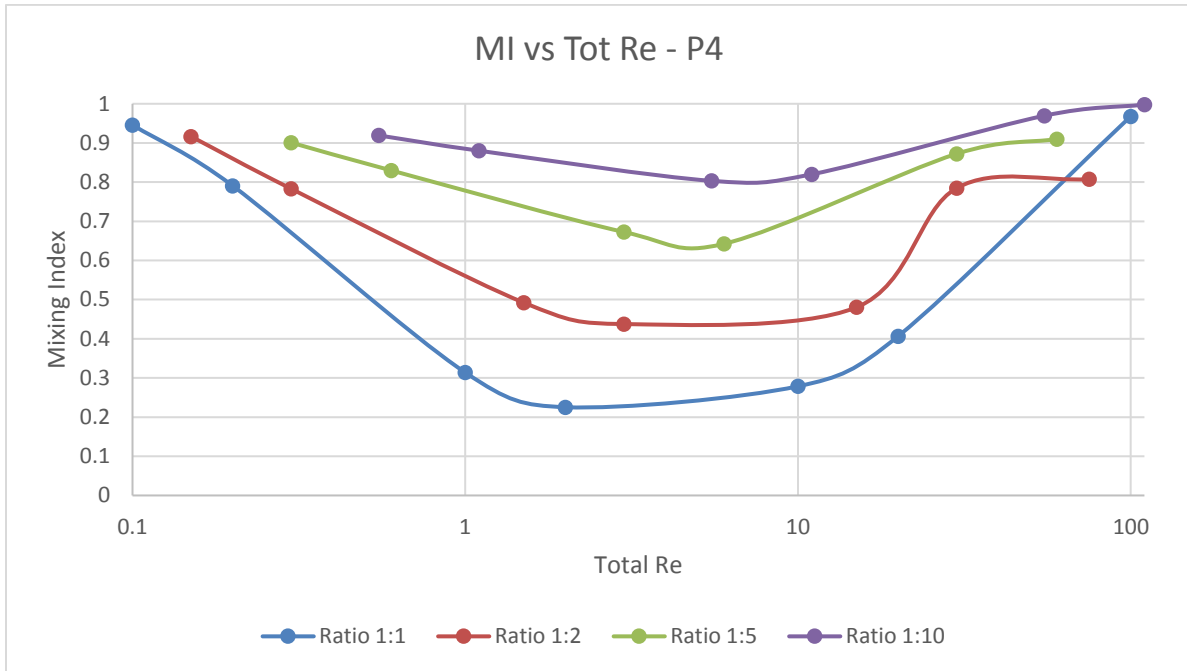
Figure 26: Mixing Indices for All Cases at Point 4

5.2.2: Entropy Generation

Higher values of $\dot{S}'''$ in cases with similar Re_T indicate superior mixing effectiveness. Plots of all the different ratios along the length of the model look fundamentally similar, as illustrated by Figure 27-29.
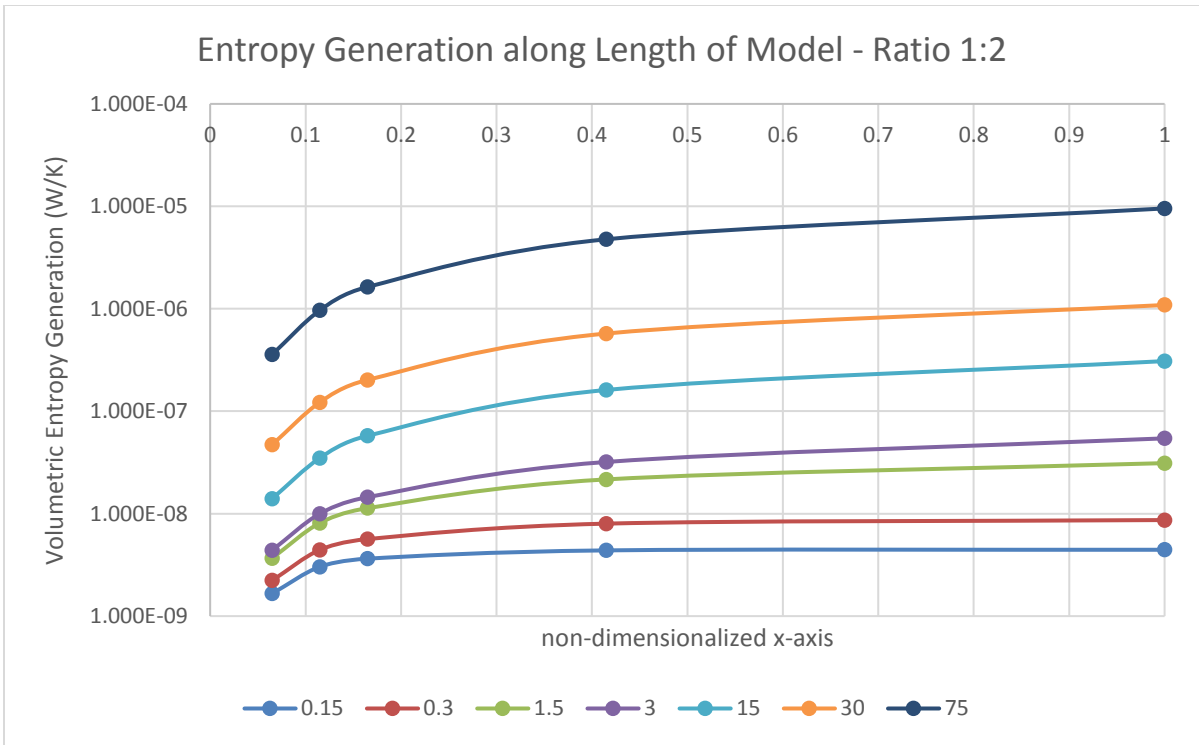
Figure 27: Entropy Generation Along Length - Ratio 1:2
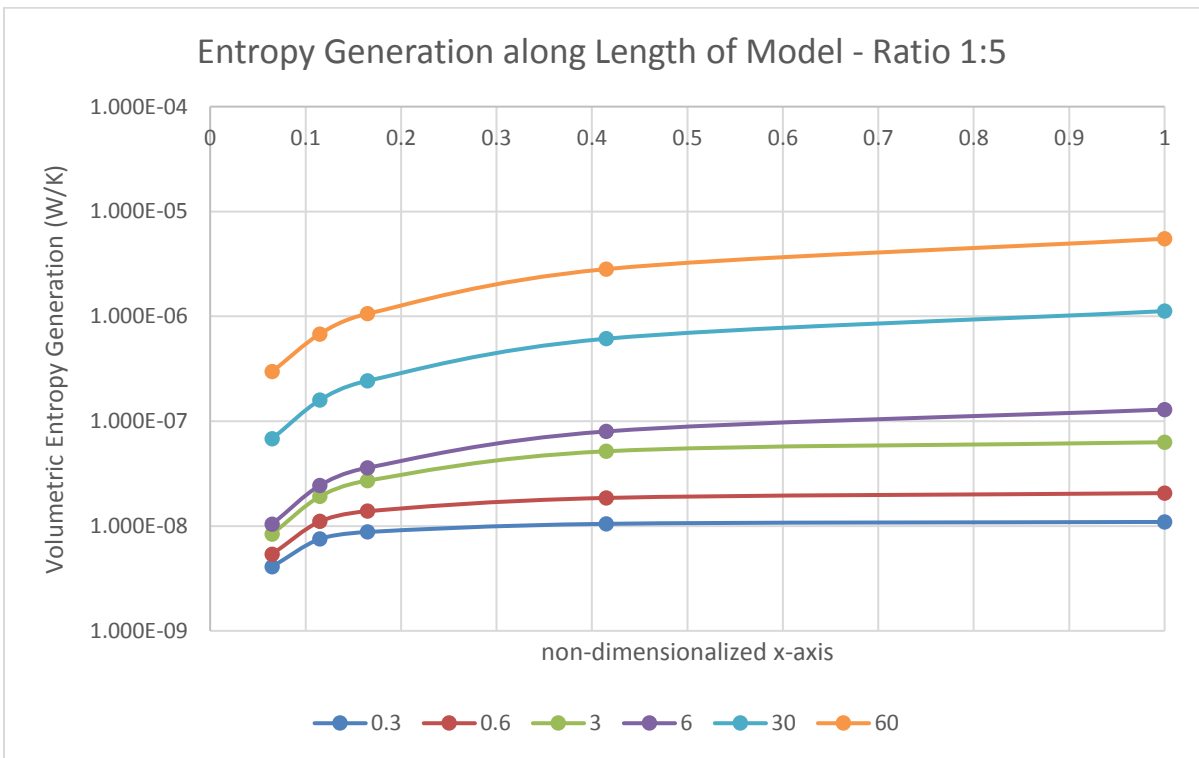
Figure 28: Entropy Generation Along Length - Ratio 1:5
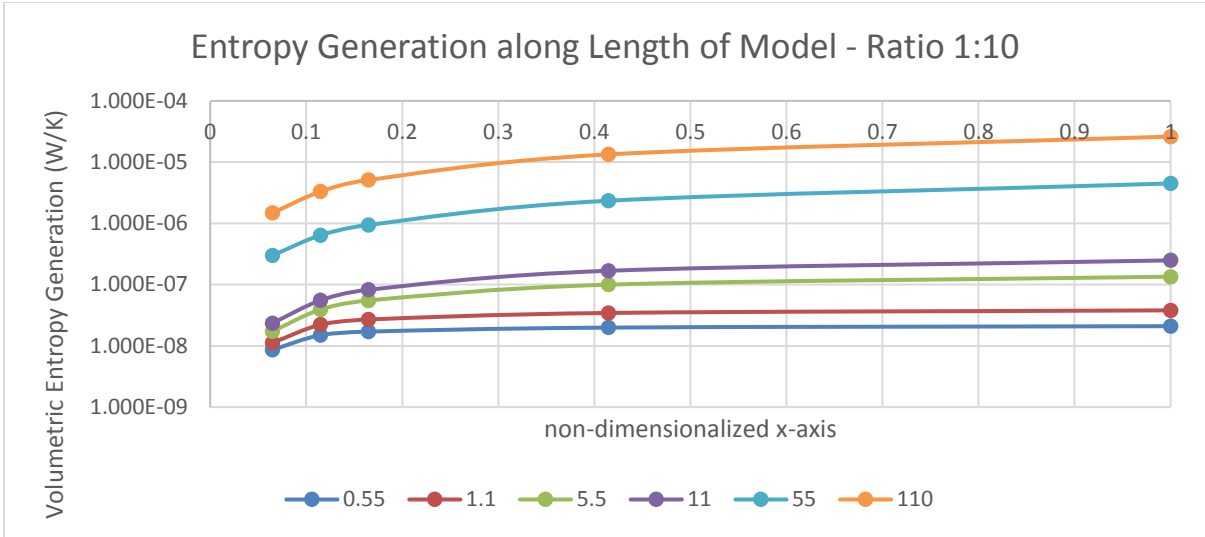
Figure 29: Entropy Generation Along Length - Ratio 1:10
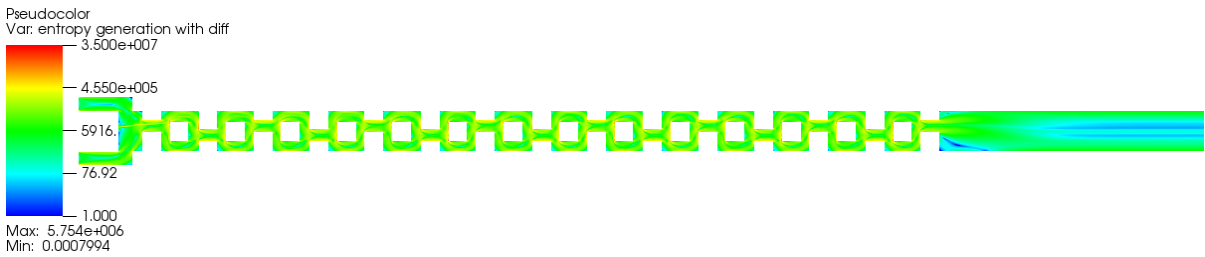
Figure 30: Entropy Generation in Midplane of Case Re10Re20
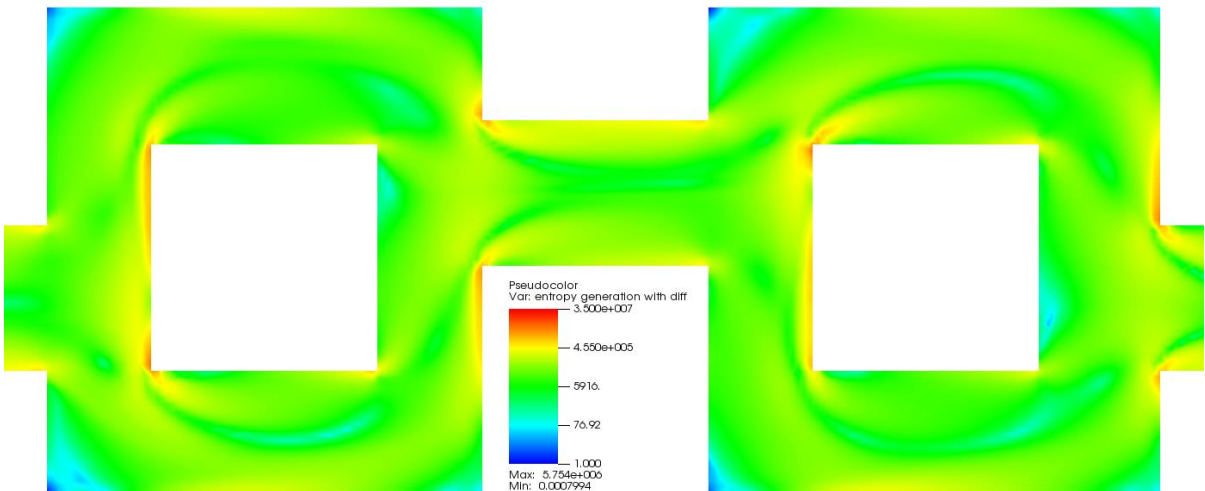
Figure 31: Entropy Generation in Midplane of Case Re10Re20 - Detail Near Point 4
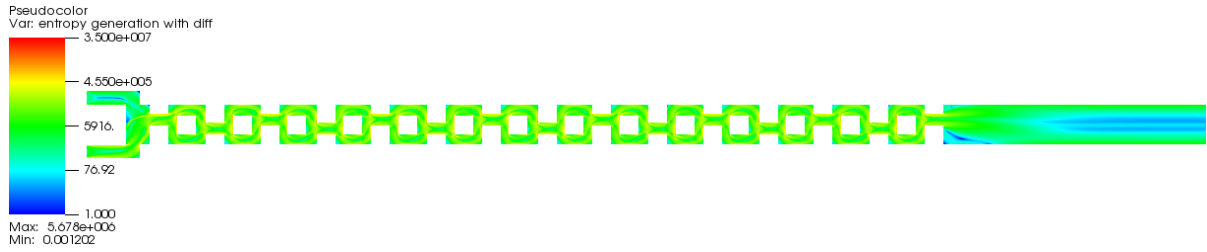
Figure 32: Entropy Generation in Midplane of Case Re5Re25
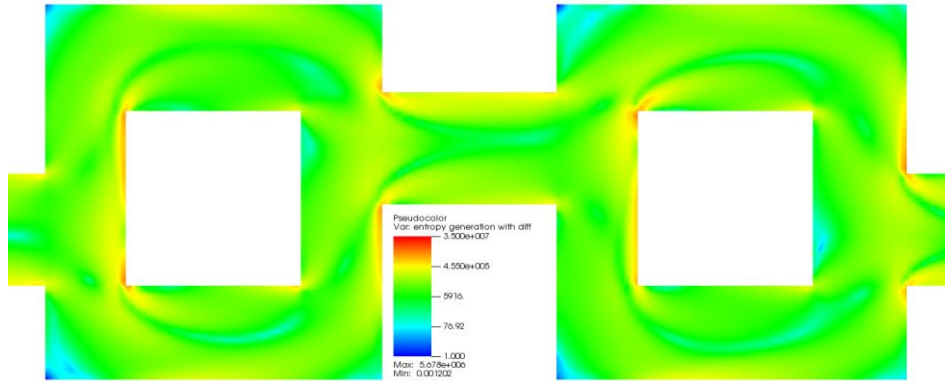
Figure 33:Entropy Generation in Midplane of Case Re5Re25 - Detail Near Point 4
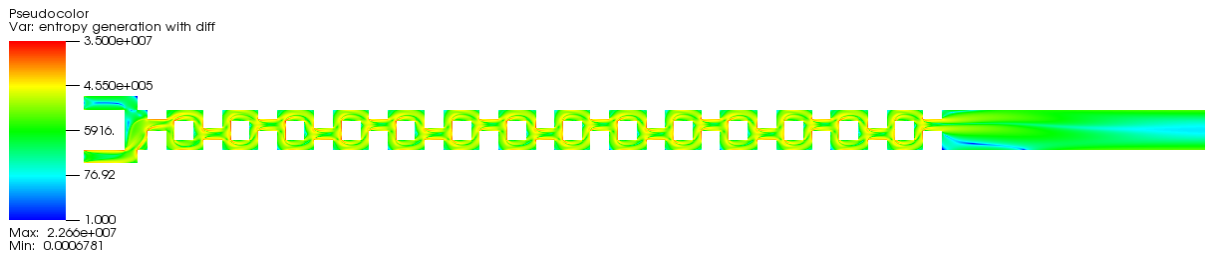
Figure 34: Entropy Generation in Midplane of Case Re5Re50
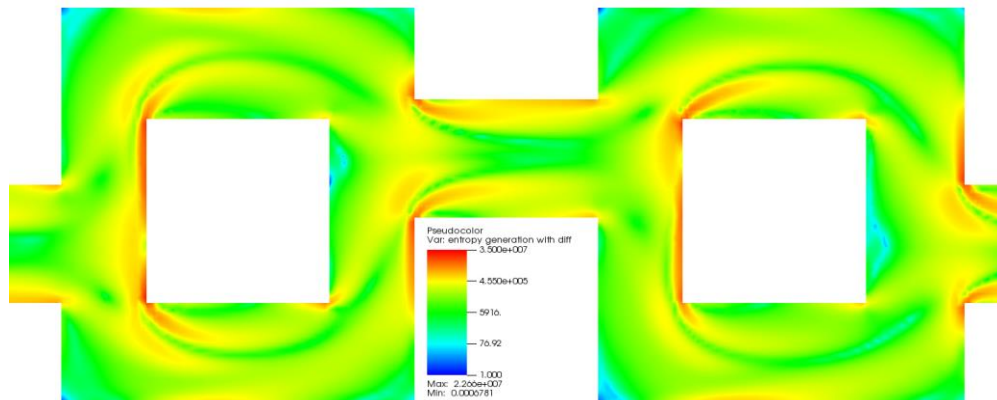
Figure 35: Entropy Generation in Midplane of Case Re5Re50 - Detail Near Point 4

42

An interesting result appears when the cases are compared at the selected representative point. In the resulting log-log plot, Figure 36, a trend is clear.
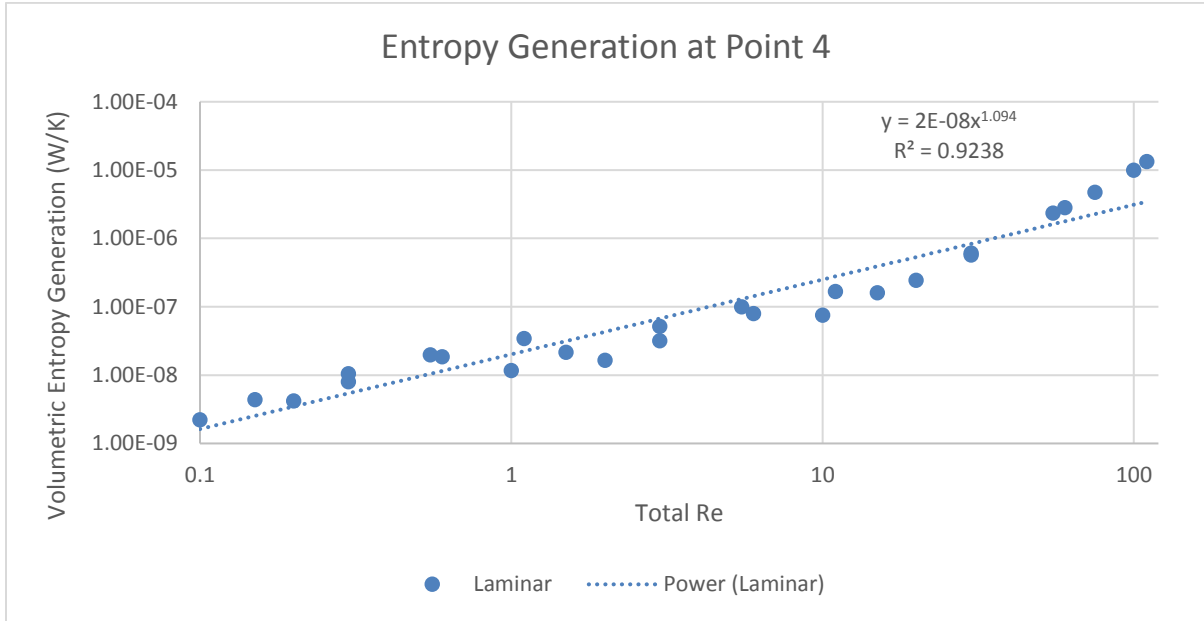
Figure 36: Log-Log Plot of Entropy Generation at Point 4 for All Cases

In attempting to formulate an analytic relationship between Re_T and $\dot{S}'''$, there is value in determining the relationship for the separated viscous and diffusive terms, as it is seen that the significance of diffusion can change depending on Re_T. Figure 37, shows the composition of the data in Figure 36 based on the contributions from the separated terms.
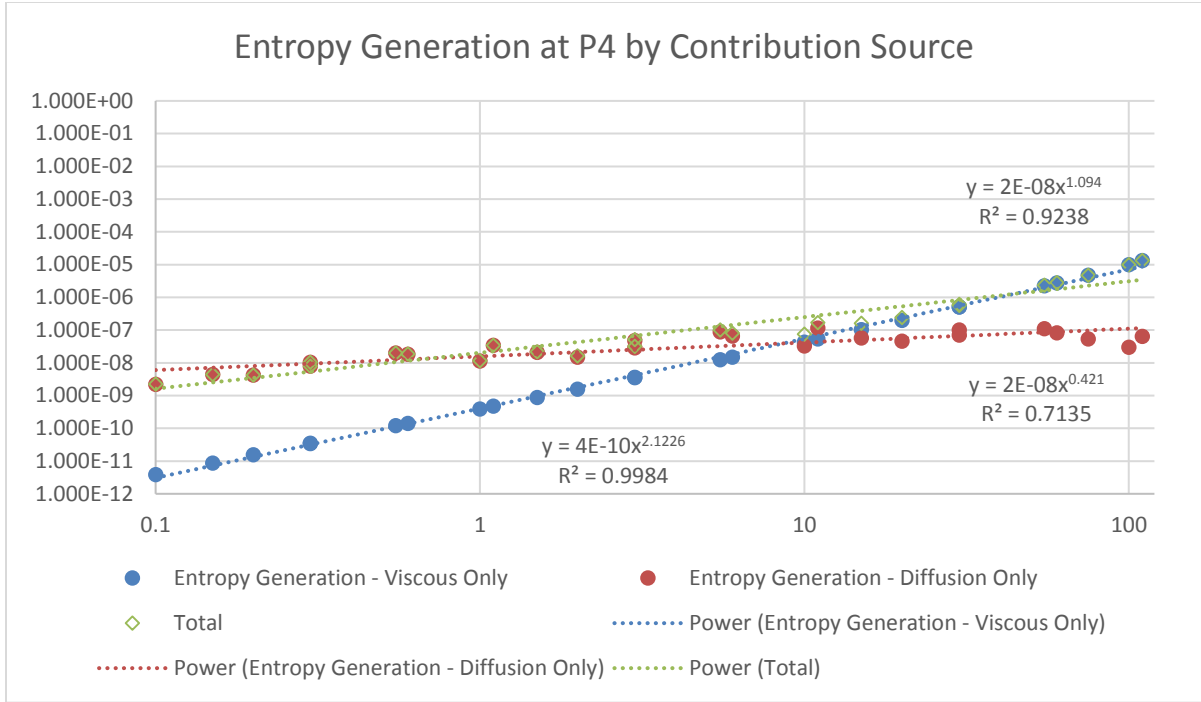
Figure 37: Entropy Generation by Term at Point 4

Recalling Equation 2.12, it is now possible to construct the following relationships:

$$\dot{S}_F''' = 4\text{x}10^{-10}Re_T{}^{2.1226} \tag{5.1}$$

$$\dot{S}_D''' = 2\text{x}10^{-8}Re_T{}^{0.421} \tag{5.2}$$

These equations are only valid for this particular model, though they hold for all laminar flow parameters.

5.3: MI vs Entropy

A relationship was also sought between Mixing Index and $\dot{S}'''$. First, it is helpful to visualize what this relationship might look like with a plot. In Figure 38, each flow ratio is separated onto its own curve for ease of reading.
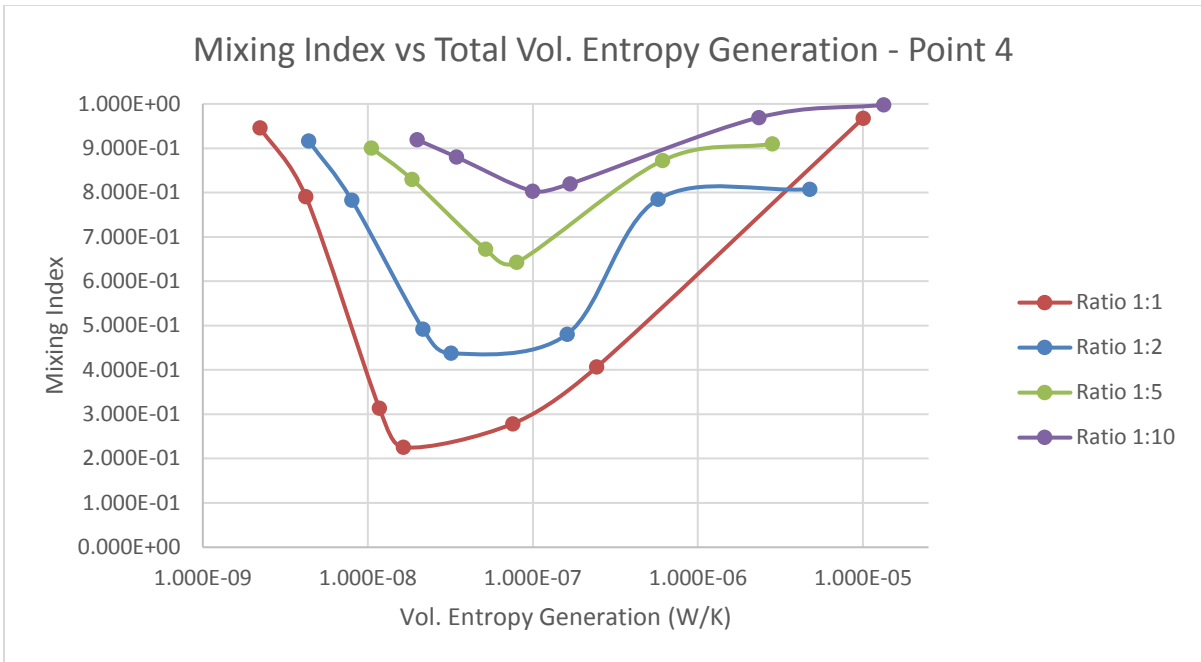
Figure 38: MI vs EntGen for All Cases at Point 4

As before, each of these can be further broken down into a contribution from viscous factors and from diffusive factors.
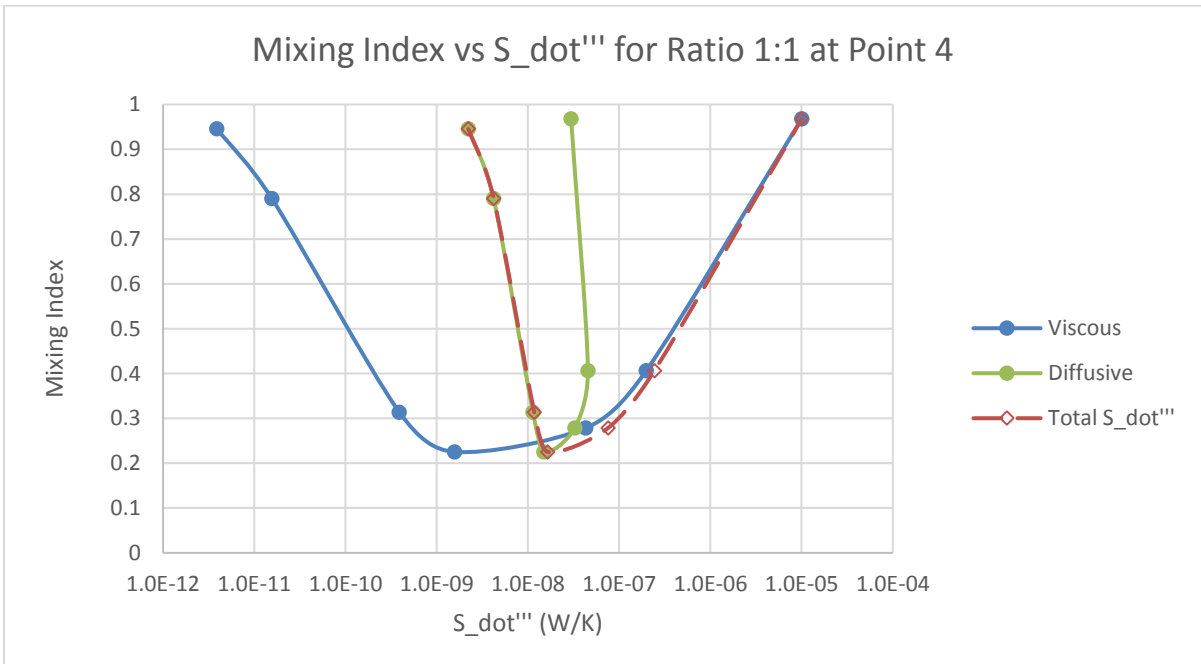
Figure 39: MI vs EntGen by Term for Ratio 1:1 at Point 4

This illustrates again that the viscous term and diffusive term swap their dominance, depending on Re_T. Using these data and Excel's Solver tool, utilizing the Generalized Reduced Gradient algorithm [46], an equation can be found for $\dot{S}'''$ as it relates to the Mixing Index. First, the equation for the 1:1 cases, as each ratio of inlets will necessitate its own equation.

$$MI = 1\text{x}10^{-11}\dot{S}'''^{-1.25} - 5.59\dot{S}'''^2 + 6.78\text{x}10^4\dot{S}''' + 0.290. \qquad (5.3)$$
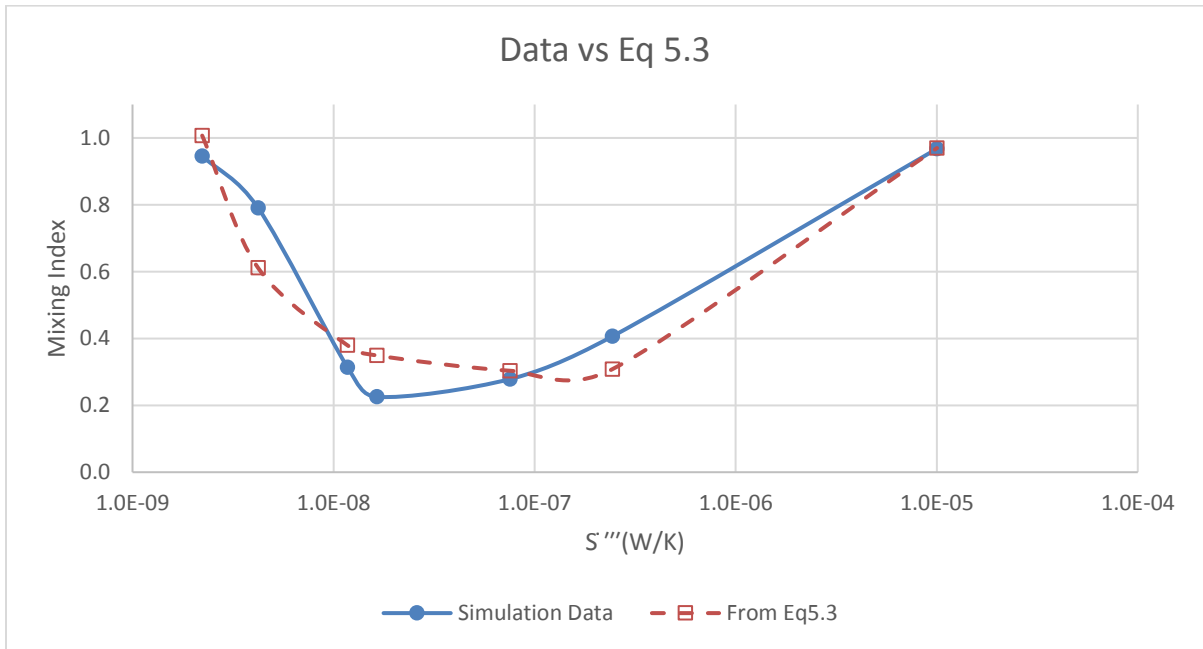
Figure 40: Simulation Data (Blue) vs Eq 5.3 (Red)

Figure 40 indicates that Equation 5.3 is in good agreement with the simulation data. For ratio 1:2 we can then obtain

$$MI = 1.52\text{x}10^{-10}\dot{S}'''^{-1.12} + 9.97\text{x}10^4\dot{S}''' + 6.78\text{x}10^4\dot{S}''' + 0.515. \qquad (5.4)$$
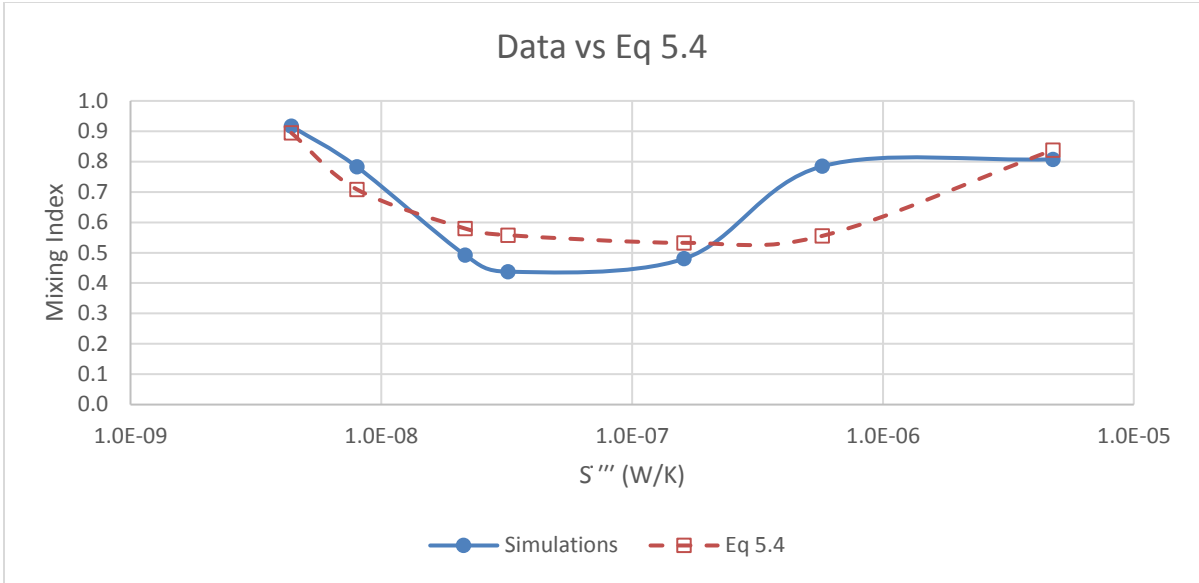
Figure 41: Simulation Data (Blue) vs Eq 5.4 (Red)

For the 1:5 cases, we get

$$MI = 0.166\dot{S}'''^{-0.122} - 3.10\text{x}10^{11}\dot{S}'''^{2} + 1.15\text{x}10^{6}\dot{S}''' - 0.672. \tag{5.5}$$
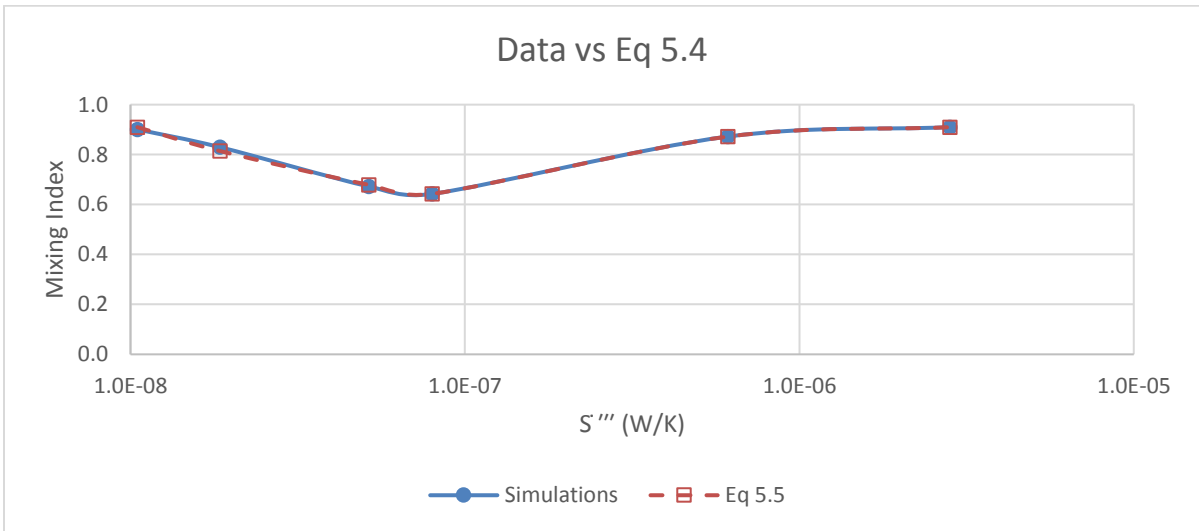
Figure 42: Simulation Data (Blue) vs Eq 5.5 (Red)

Finally, for the 1:10 ratio cases, we obtain

$$MI = 0.259\dot{S}'''^{-0.073} - 9.95\text{x}10^{9}\dot{S}'''^{2} + 1.66\text{x}10^{5}\dot{S}''' - 0.032. \tag{5.6}$$
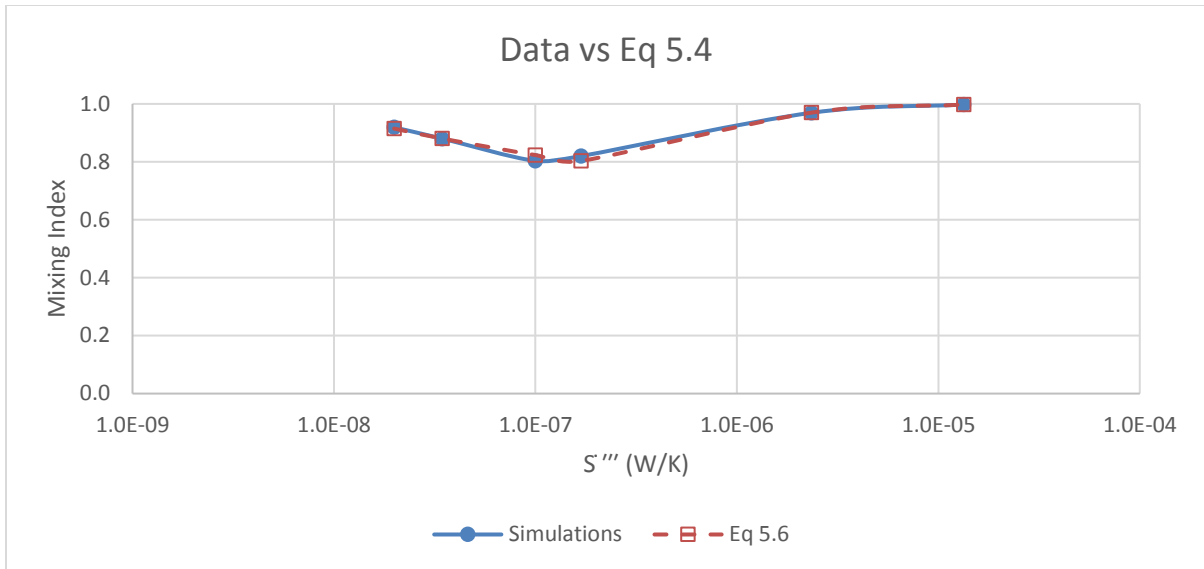
Figure 43: Simulation Data (Blue) vs Eq 5.6 (Red)

Excel's Solver was particularly adept at finding solutions for the 1:5 and 1:10 cases, due to those ratios having 1 fewer data point to fit than the 1:1 and 1:2 ratios. The sum of squares obtained by the least squares method for all of the solutions above is below 0.09.

Equations 5.3-5.6 are, like all of the equations obtained in this chapter, specific to the model used in the simulations. They are valid for the flow parameters in laminar simulations run in this thesis.

5.4 Turbulent Cases

High Re simulations are uncommon in microchannels, but this thesis sought to explore the upper end of flow rates typically used in these applications. All attempts to run simulations with $Re_T > 110$ met with failures to converge. Enabling Fluent's turbulent k-epsilon solver allowed these simulations to run to convergence. While Mixing Indices and entropy generation rates were calculated for these simulations, no attempt is made here to further characterize these simulations.

5.4.1 Mixing Efficiency

Mixing Index values are presented here identically to the way they were displayed in Section 5.1.1 for ease of comparison.
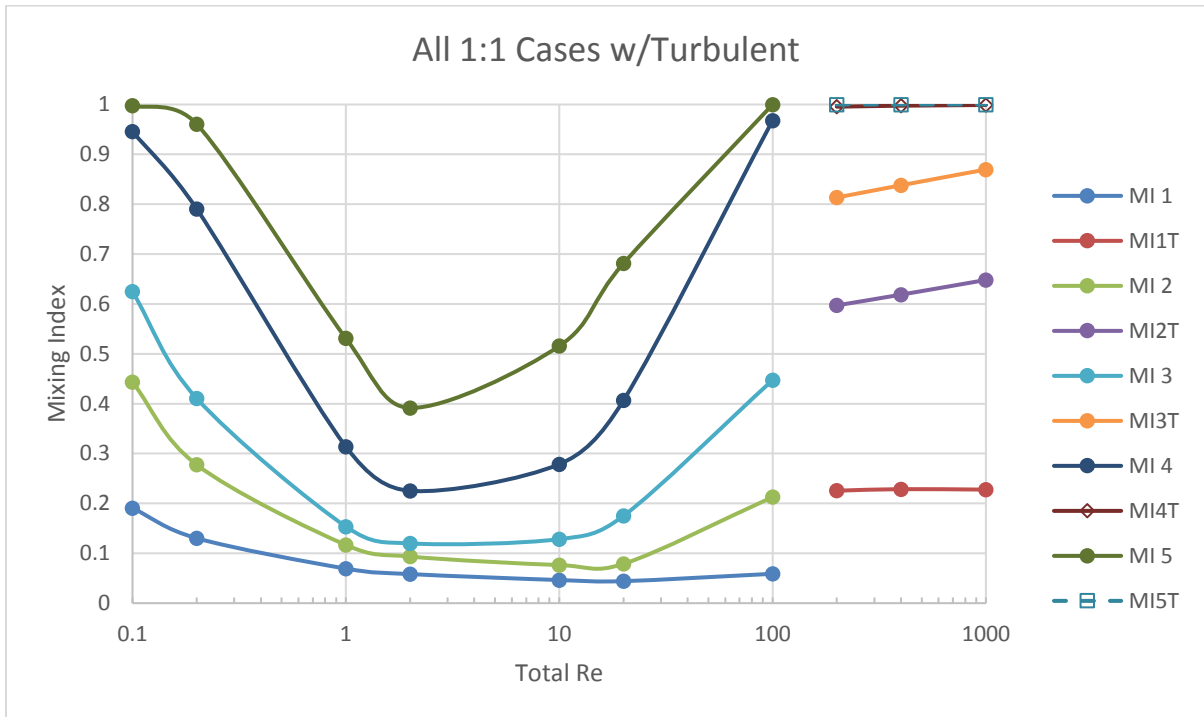
Figure 44: Mixing Index vs Total Re for all 1:1 Cases
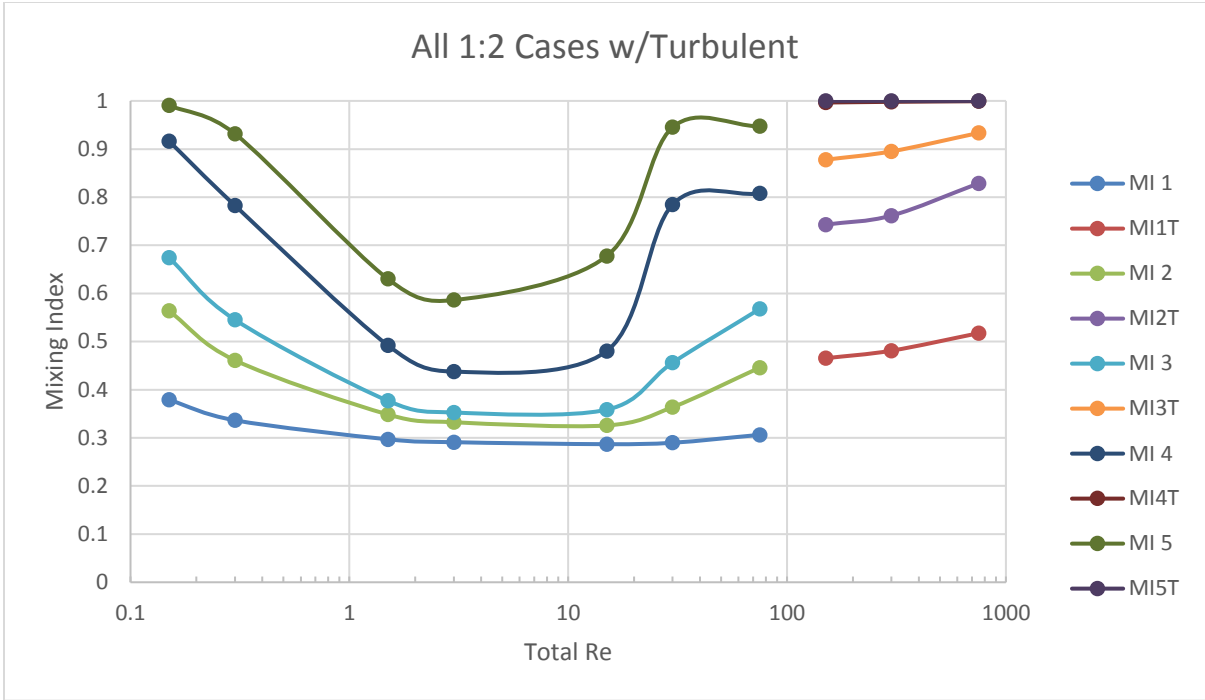
Figure 45: Mixing Index vs Total Re for all 1:2 Cases
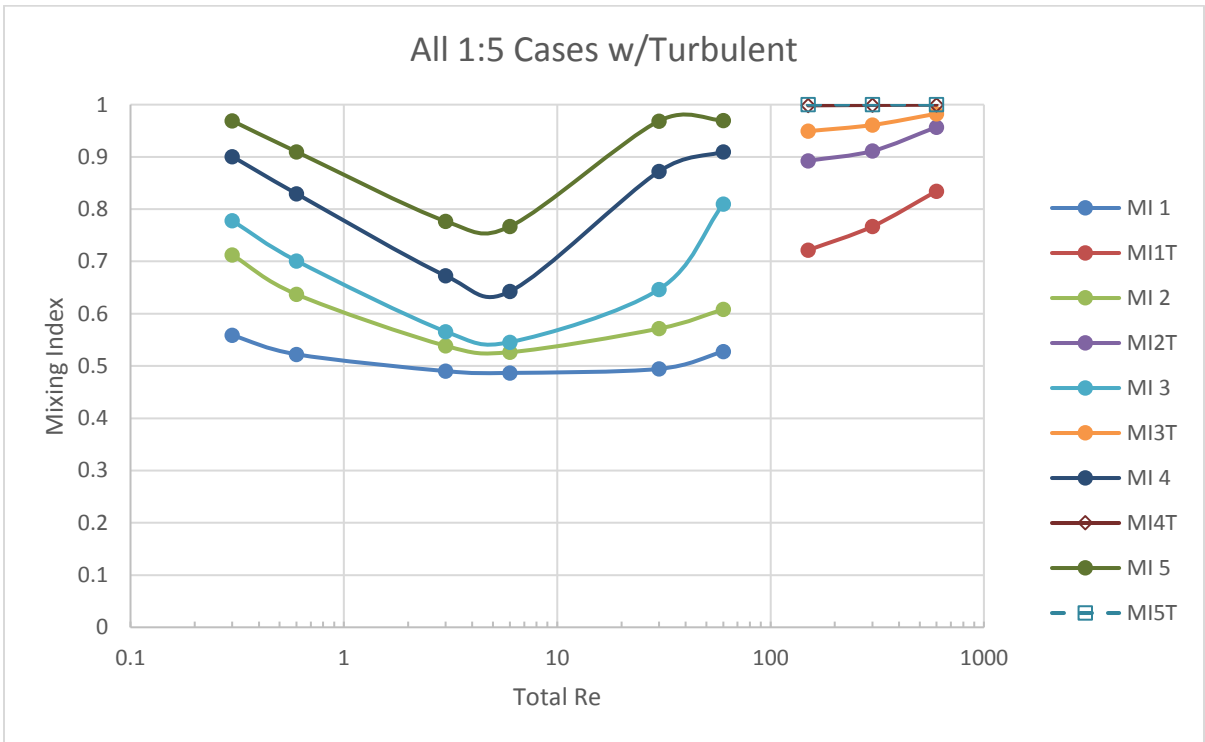
Figure 46: Mixing Index vs Total Re for all 1:5 Cases
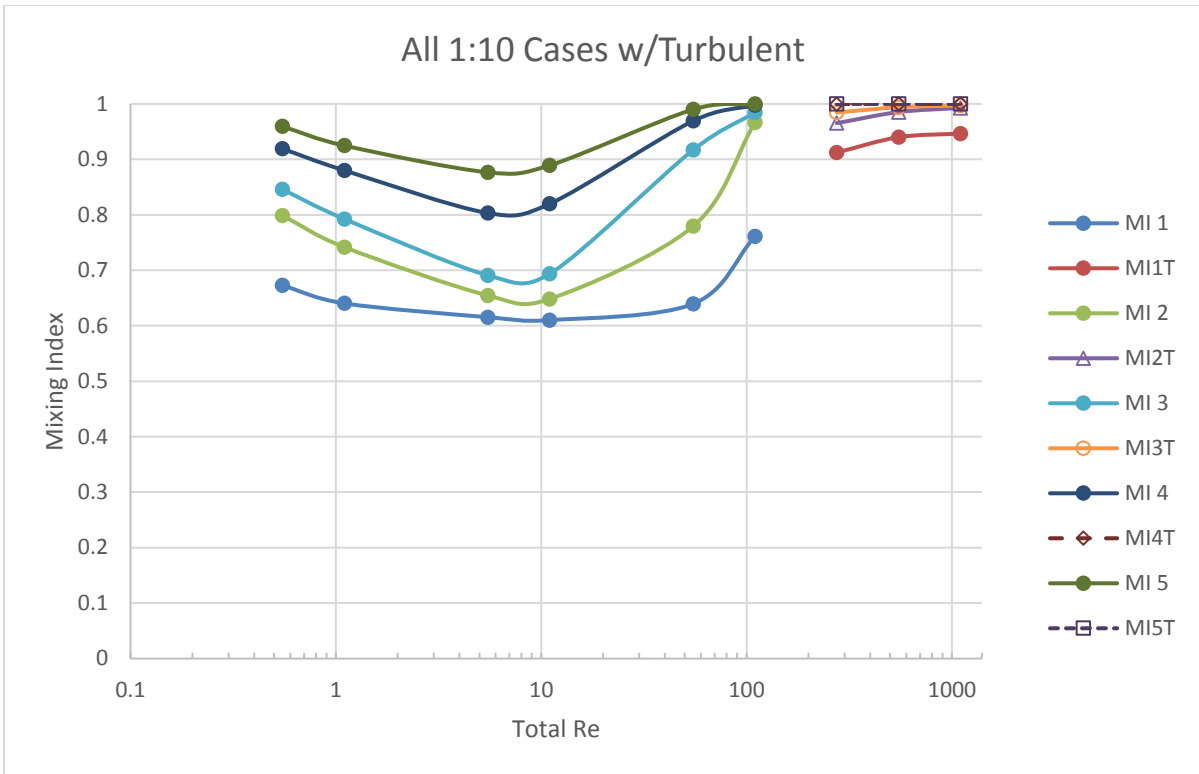
Figure 47: Mixing Index vs Total Re for all 1:10 Cases

These plots illustrate that mixing is extremely good when flow becomes turbulent inside this mixer design. In all turbulent cases, MI>0.995 by the time flow reaches Point 4.

5.4.2 Entropy Generation

As Figure 48 reveals, $\dot{S}'''$ for turbulent cases is almost perfectly logarithmic in these simulations.
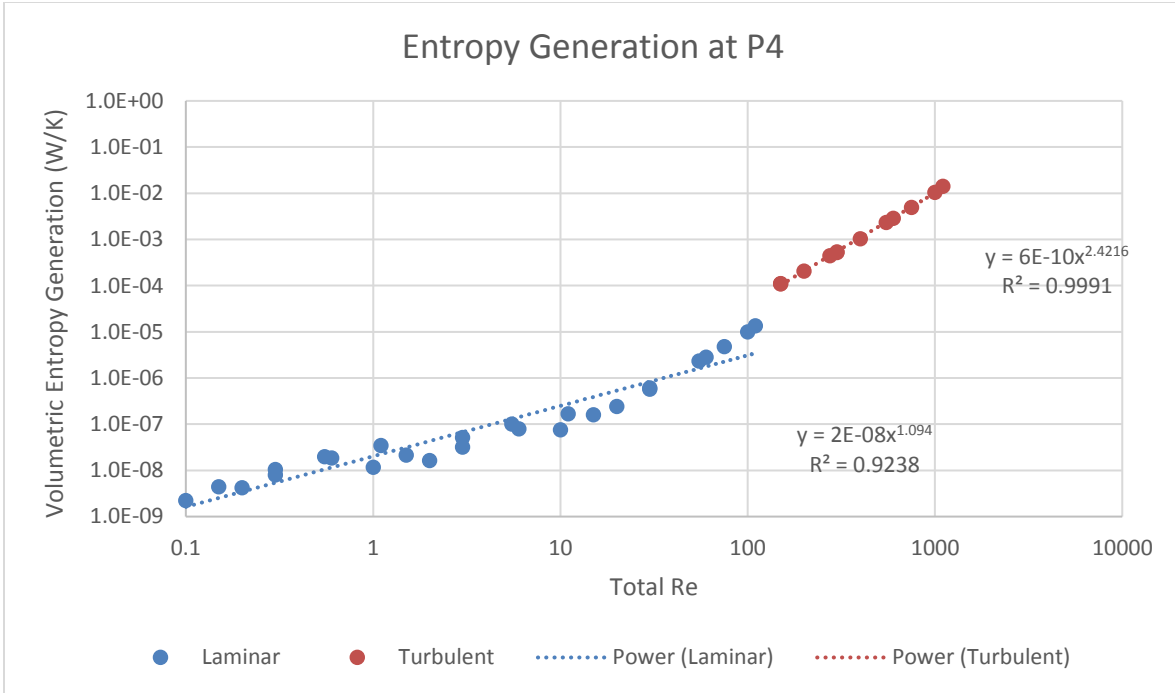
Figure 48: Volumetric Entropy Generation Rate vs Total Re for All Cases

As in the laminar cases it is possible to identify contributions from different terms to $\dot{S}'''$. In

turbulent cases the term calculated from Equation 2.14 is added to the total value.
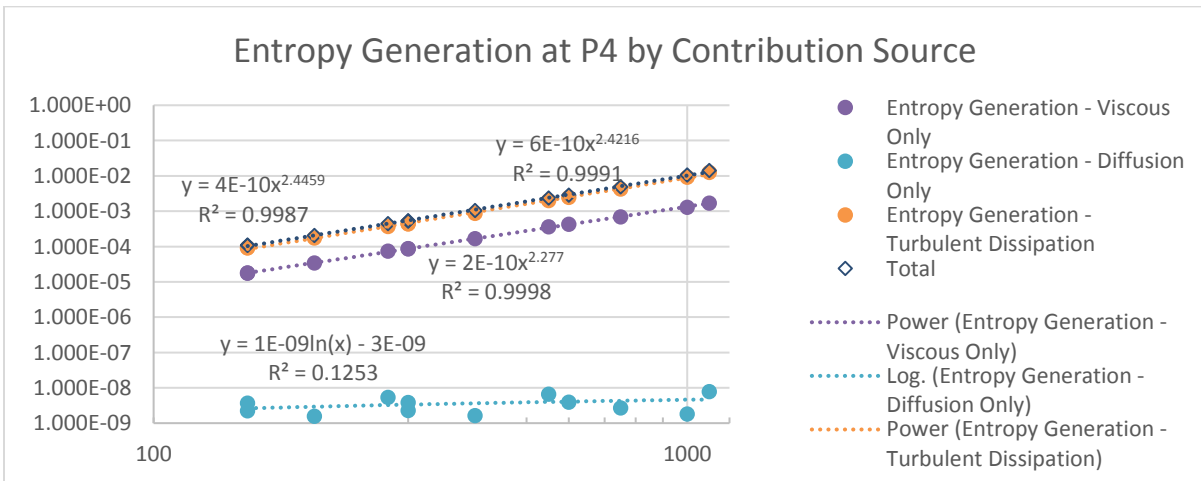
Figure 49: Entropy Generation Contribution by Source Term for Turbulent Cases

As might have been expected based on the laminar cases, the diffusive term contributes so

little to the total value of $\dot{S}'''$ that it is negligable. Instead, turbulent dissipation dominates.
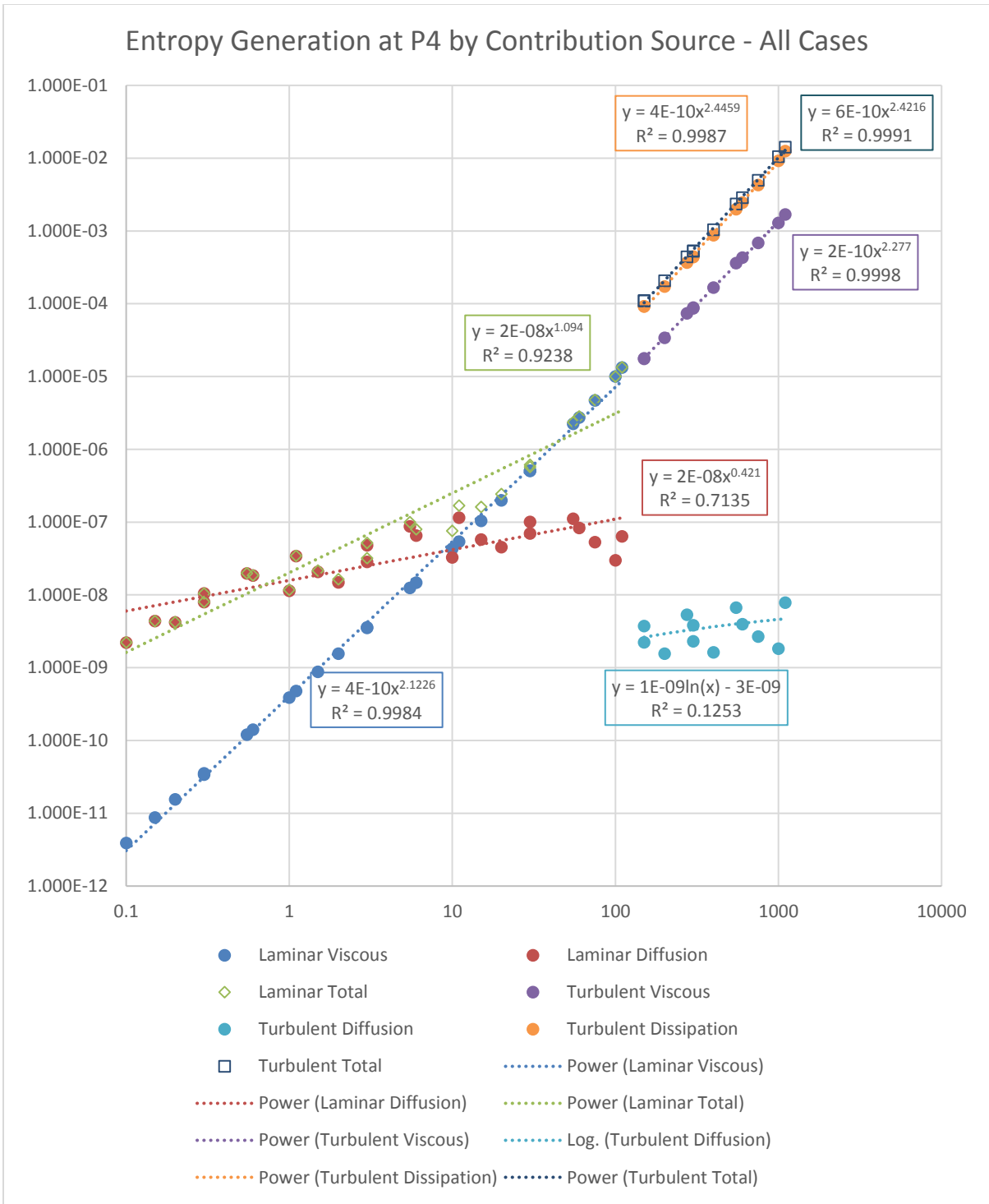
Figure 50: Entropy Generation by Source Term for All Cases

Chapter 6: Conclusion

This thesis investigated the effectiveness of a particular micromixing design and detailed the design and set-up of the numerical simulations conducted to that end. Twenty-six laminar and an additional twelve turbulent simulations were run on a supercomputer cluster to explore the characteristics of the model geometry.

A deep dive into Fluent's mathematical underpinnings was conducted. This investigation into the workings of the simulation software led to performance savings in the simulation phase of the thesis by determining that it was possible to disable the energy solver, which is enabled by default alongside the species transport solver.

Several analytical relationships were found between flow characteristics, volumetric entropy generation rate, and a mixing index. These relationships allow for the easy prediction of mixing effectiveness of this micromixer design based on to total inlet Reynolds number and the flow ratio of the inlets. Additionally, an unexpected turbulent mixing regime was discovered in the course of running the simulations.

There is more yet unknown about this particular mixer design. A more thorough investigation of its turbulent characteristics is certainly an area for future research. Flow velocities sufficient to cause turbulence are not typically used in micromixers, but this mixer design generated turbulence at a lower Reynolds number than was expected. It may be desirable to run the mixer at those velocities in specific applications. An experimental verification of the results of this thesis is also called for. Simulations or experiments including substances other than water also offer areas for further work.

References

[1] G. S. Jeong, S. Chung, C. B. Kim and S. H. Lee, "Applications of Micromixing Technology," *Analyst,* vol. 153, no. 3, pp. 460-473, 2010.

[2] J. P. Lafleur, A. Jönsson, S. Senkbeil and J. P. Kutter, "Recent advances in lab-on-a-chip for biosensing applications," *Biosensors and Bioelectronics,* vol. 76, pp. 213-233, 2015.

[3] J. Y. Yoon and B. Kim, "Lab-on-a-Chip Pathogen Sensors for Food Safety," *Sensors,* vol. 12, pp. 10713-10741, 2012.

[4] C. Y. Lee, C. L. Chang, Y. N. Wang and L. M. Fu, "Microfluidic Mixing: A Review," *International Journal of Molecular Sciences,* vol. 12, no. 5, pp. 3263-3287, 2011.

[5] P. Gravesen, J. Branebjerg and O. S. Jensen, "Microfluidics - a review," *Journal of Micromechanics and Microengineering,* vol. 3, no. 4, p. 168, 1993.

[6] A. Fick, "On Liquid Diffusion," *The London, Edinburgh, and Dublin Philisophical Magazine and Journal of Science,* vol. X, pp. 30-39, 1855.

[7] W. Buchegger, C. Wagner, B. Lendl, M. Kraft and M. J. Vellekoop, "A Highly Uniform Lamination Micromixer with Wedge Shaped Inlet Channels for Time Resolved Infrared Spectrocopy," *Microfluidics and Nanofluidics,* vol. 10, no. 4, pp. 889-897, 2011.

[8] G. F. Naterer and J. A. Camberos, Entropy-Based Design and Analysis of Fluids Engineering Systems, Boca Raton, FL: CRC Press- Taylor & Fancis Group, 2008.

[9] P. E. Neerincx, R. P. Denteneer, S. Peelen and H. E. Meijer, "Compact Mixing Using Multiple Splitting, Stretching, and Recombining Flows," *Macromolecular Materials and Engineering,* vol. 296, no. 3-4, p. 349=361, 2011.

[10] S. Hardt, H. Pennemann and F. Schönfeld, "Theoretical and Experimental Characterization of a Low-Reynolds Number Split-and-Recombine Mixer," *Microfluidics and Nanofludics,* vol. 2, no. 3, pp. 237-248, 2006.

[11] T. R. Shih and C. K. Chung, "A High-Efficiency Planar Micromixer with Convection and Diffusion Mixing Over a Wide Reynolds Number Range," *Microfluidics and Nanofluidics,* vol. 5, no. 2, pp. 175-183, 2008.

[12] H. Song, M. R. Bringer, J. D. Tice, C. J. Gerdts and R. F. Ismagilov, "Experimental Test of Scaling of Micing by Chaotic Advection in Droplets Moving Through Microfluidic Channels," *Applied Physics Letters,* vol. 83, no. 22, pp. 4664-4666, 2003.

[13] K. Chen, H. Lu, M. Sun, L. Zhu and Y. Cui, "Mixing enhancement of a novel C-SAR microfludic mixer," *Chemical Engineering Research and Design,* vol. 132, p. 338=345, 2018.

[14] X. Shi, Y. Xiang, L. X. Wen and J. F. Chen, "CFD Analysis of Flow Patterns and Micromixing Efficiency in a Y-type Microchannel Reactor," *Industrial & Engineering Chemistry Research,* vol. 51, no. 43, pp. 13944-13952, 2012.

[15] V. Mengeaud, J. Josserand and H. H. Girault, "Mixing Processess in a Zigzag Microchannel: Finite Element Simulations and Optical Study," *Analytical Chemistry,* vol. 74, no. 16, pp. 4279-4286, 2002.

[16] A. D. Stroock, S. K. Dertinger, A. Ajdari, I. Mezic, H. A. Stone and G. M. Whitesides, "Chatic Mixer for Microchannels," *Science,* vol. 295, no. 5555, pp. 647-651, 2002.

[17] R. H. Liu, M. A. Stremler, K. V. Sharp, M. G. Olsen, J. G. Santiago, R. J. Adrian and D. J. Beebe, "Passive Mixing in a Three-Dimensional Serpentine Microchannel," *Journal of Microelectromechanical Systems,* vol. 9, no. 2, p. 190=197, 2000.

[18] R. A. Vijayendran, K. M. Motsegood, D. J. Beebe and D. E. Leckband, "Evaluation of a Three Dimensional Micromixer in a Surface-Based Biosensor," *Langmuir,* vol. 19, no. 5, pp. 1824-1828, 2003.

[19] H. Chen and J. C. Meiners, "Topologic Mixing on a Microfluidic Chip," *Applied Physics Letters,* vol. 84, no. 12, pp. 2193-2195, 2004.

[20] S. J. Park, J. K. Kim, J. Park, S. Chung, C. Chung and J. K. Chang, "Rapid Three-Dimensional Passive Rotation Micromixer Using the Breakup Process," *Journal of Micromechanics and Microengineering,* vol. 13, no. 1, p. 6, 2003.

[21] C. P. Jen, C. Y. Wu, Y. C. Lin and C. Y. Wu, "Design and Simulation of the Micromixer with Chaotic Advection in Twisted Microchannels," *Lab on a Chip,* vol. 3, no. 2, pp. 77-81, 2003.

[22] A. M. Gillispie, "Determination of an Analytical Relationship between Entropy Generation and Mixing Efficiency for Micromixer Applications," M.S. thesis,

Department of Engineering and Physics, Univ. of Central Oklahoma, Edmond, OK, 2017.

[23] A. Einstein, "On the motion of small particles suspended in liquids at rest required by the molecular-kinetic theory of heat," *Annalen der physik,* vol. 17, no. 1, pp. 549-560, 1905.

[24] R. Miyake, T. S. Lammerink, M. Elwenspoek and J. H. Fluitman, "Micro Mixer with Fast Diffusion," *Proceedings IEEE Micro Electro Mechanical Systems,* pp. 248-253, 1993.

[25] F. M. White, Viscous Fluid Flow, 3rd ed., New York, NY: McGraw-Hill Higher Education, 2011.

[26] B. Schmandt, V. Iyer and H. Herwig, "Determination of Head Change coefficients for Dividing and Combining Junctions: A method based on the Second Law of Thermodynamics," *Chemical Engineering Science,* vol. 111, pp. 191-202, 2014.

[27] S. E. Ferguson, Jr., E. C. Lemley and M. R. Hossan, "Second Law Analysis of Passive Micro-Mixing in Rectangular Microchannels with Flow Obstacles," *ASME International Mechanical Engineering Congress and Exposition,* vol. 7: Fluids Engineering, p. V007T09A056, 2017.

[28] B. Schmandt and H. Herwig, "Loss Coefficients in Laminar Flows: Essential for the Design of Micro Flow Systems," *PAMM,* vol. 11, no. 1, pp. 27-30, 2011.

[29] S. Del Giudice, C. Nonino and S. Savino, "Effects of Viscous Dissipation and Temperature Dependent Viscosity in Thermally and Simultaneously Developing Laminar Flows in Microchannels," *International Journal of Heat and Fluid Flow,* vol. 28, no. 1, pp. 15-27, 2007.

[30] D. M. McEligot, E. J. Walsh, E. Laurien and P. R. Spalart, "Entropy Generation in the Viscous Parts of Turbulent Boundary Layers," *Journal of Fluids Engineering,* vol. 130, no. 6, p. 061205, 2008.

[31] H. Childs et al., "Visit: An End-User Tool For Visualizing and Analyzing Very Large Data.," *High Performance Visualization–Enabling Extreme-Scale Scientific Insight,* pp. 357-372, Oct 2012.

[32] S. Hossain, A. Husain and K. Y. Kim, "Optimization of Micromixer with Staggered Herringbone Grooves on Top and Bottom Walls," *Engineering Applications of Computational Fluid Mechanics,* vol. 5, no. 4, pp. 506-516, 2011.

[33] S. Chou, Y. Song and S. Hsiau, "A Study of the Mixing Index in Solid Particles," *KONA Powder and Particle Journal,* vol. 34, no. 1, pp. 275-281, 2016.

[34] P. M. C. Lacey, "The Mixing of Solid Particles," *Chemical Research and Design,* vol. 75, no. 1, pp. S49-55, 1997.

[35] A. Bejan, Convection Heat Transfer, 4th, Ed., Hobooken, NJ: John Wiley & Sons, 2013.

[36] M. Saffaripour and R. Culham, "Measurement of Entropy Generation in Microscale Thermal-Fluid Systems," *Journal of Heat Transfer,* vol. 132, no. 12, 2010.

[37] M. Mourad, A. Hassen, N. Hidouri and B. B. Ammar, "Second Law Analysis in Convective Heat and Mass Transfer," *Entropy,* vol. 8, no. 1, pp. 1-17, 2006.

[38] J. O. Hirschelder, C. F. Curtis and R. B. Bird, Molecular Theory of Gases and Liquids, New York, NY: Wiley, 1954.

[39] F. Kock and H. Herwig, "Entropy production calculation for turbulent shear flows and their implementation in cfd codes," *International Journal of Heat and Fluid Flow,* vol. 26, pp. 672-680, 2005.

[40] J. H. Wang, "Self-Diffusion Coefficients of Water," *The Journal of Physical Chemistry,* vol. 69, no. 12, p. 4412, 1965.

[41] IUPAC, IUPAC. Compendium of Chemical Terminology, 2nd ed. (the "Gold Book"). Compiled by A. D. McNaught and A. Wilkinson. Blackwell Scientific Publications, Oxford (1997). Online version (2019-) created by S. J. Chalk. ISBN 0-9678550-9-8.

[42] Ansys, Inc., *Ansys® Fluent 16.1: Theory Guide,* Canonsbburg, PA, 2015.

[43] T. Barth and D. Jespersen, "The Deisgn and Application of Upwind Schemes on Unstructured Meshes," in *AIAA 27th Aerospace Sciences Meeting*, Reno, 1989.

[44] Lawrence Livermore National Laboratory, "The VisIt User Manual," Lawrence Livermore National Laboratory, 2017. [Online]. Available: https://visit-sphinx-github-user-manual.readthedocs.io/en/latest/index.html.

[45] E. C. Lemley, "sdot_rect_duct," 18 April 2019. [Online]. Available: https://docs.google.com/spreadsheets/d/1ycZelhYouhI_ Y3mK0BC9z17PfwrV5h0LbSFZ74N39RU. [Accessed 18 April 2019].

[46] Frontline Systems, Inc., "Standard Excel Solver - Limitations of Nonlinear Optimization," Frontline Systems, Inc., [Online]. Available: https://www.solver.com/standard-excel-solver-limitations-nonlinear-optimization. [Accessed May 2020].

Appendix 1: File Naming Conventions and Script Examples

File names for a particular case used the case names described in Tables 2-5 of section 4.6 as their base. An error found with the diffusion coefficient after completing the first run of simulations led to a second set of case files being created with the letters `upD` (for updated D) appended to the case name. For ease of navigation, files were separated into three main directories. `sameinlets` contained cases with the same inlet velocities. `ReLow` contained cases where at least one of the inlets was no higher than Re=5. `ReHigh` contained all other cases, including turbulent cases in a `turb` subdirectory. A fourth `meshstudy` high-level directory was used for the various mesh study simulations and the value testing simulations described in section 4.3 and 4.5.

Each case required the creation of a minimum of 3 files, but more often 5 files were created. Each had the case name as a base and one of the following five extensions: `.cas`, `.in`, `.dat`, `.out`, or `.err`. In many instances these were also accompanied by a .sbatch script file for running with Buddy's scheduling system, Slurm Workload Manager, though this practice was altered after determining it was possible to group several cases together into a single batch file by utilizing SLURM's job array features without running out of Fluent licenses.

A1.1: Example `.sbatch` file

Files of the .sbatch format are specialized bash script files and as such follow many, though not all, of the same syntax. The following .sbatch file will create a job array of 10 jobs, name it "fluent-runs", use 60 Fluent licenses, and split the work between 3 of Buddy's nodes. It

will attempt to load in the first 10 .in files it finds in the directory to run with Fluent. It will

only run a single Fluent task at a time, which prevents it from running out of licenses.

```
#!/bin/bash

#SBATCH --job-name=fluent-runs

#SBATCH -o %A-%a.out

#SBATCH -p nodes

#SBATCH -e %A-%a.err

#SBATCH -n 60 --tasks-per-node=20

#SBATCH --array=1-10%1


arrayfile=(*.in)

/ansys_inc/v161/fluent/bin/fluent 3ddp -g -slurm -t60 -pinfiniband -
i "${arrayfile[$SLURM_ARRAY_TASK_ID-1]}"
```

Note that this will result in .out and .err files that are not named according to the case file, but

rather according to the Slurm job and task IDs. This is normally of no consequence, as the

error files are typically empty and the output file contains only information about residual

values per iteration and other compute-time information. If, for whatever reason, it was

desired to rename the .err and .out files to match the other files for a particular case, the

following bash script will identify the case name from a .out file, and rename the

associated .out and .err files.

```sh
#!/bin/sh

for f in *.out

do

  read -r var1 var2 var3 var4 var5 var6 var7 var8 newname < "$f"

  if [ ! -f "${newname%.in}.out" ]

    then

      echo "File name $newname detected in file $f. Renaming to
${newname%.in}.out"

      mv "$f" "${newname%.in}.out"

      echo "Also renaming ${f%.out}.err to ${newname%.in}.err"

      mv "${f%.out}.err" "${newname%.in}.err"

    else

      echo "File '${newname%.in}.out' already exists. Skipped '$f'
and its error file."

  fi

done
```

Appendix 2: Validity of Disabling the Energy Solver

Table 7: Mixing Index with Energy Solver

Energy Solver Enabled		
Coordinates	Variance	MI
0.00004	2.10E-01	0.083594
0.00025	1.42E-01	0.246239
0.00046	5.59E-02	0.527208
0.00067	1.65E-02	0.743317
0.00088	4.13E-03	0.871539
0.00109	6.52E-04	0.948924
0.00130	3.05E-04	0.965052
0.00151	1.30E-04	0.977216
0.00172	2.41E-05	0.99019
0.00193	4.26E-06	0.995872
0.00214	1.56E-06	0.997499
0.00235	8.97E-07	0.998106
0.00256	3.59E-07	0.998802
0.00277	3.61E-08	0.99962
0.00298	2.38E-09	0.999902
0.00349	1.96E-10	0.999972

Table 8: Mixing Index without Energy Solver

Energy Solver Disabled			
Coordinates	Variance	MI	%diff
0.00004	2.10E-01	0.083594	0.000E+00
0.00025	1.42E-01	0.246239	0.000E+00
0.00046	5.59E-02	0.527211	5.617E-06
0.00067	1.65E-02	0.743317	0.000E+00
0.00088	4.13E-03	0.871538	-8.932E-07
0.00109	6.52E-04	0.948925	3.301E-07
0.00130	3.05E-04	0.965052	2.372E-07
0.00151	1.30E-04	0.977216	8.983E-08
0.00172	2.41E-05	0.99019	-2.059E-08
0.00193	4.26E-06	0.995872	-4.865E-08
0.00214	1.56E-06	0.997499	-2.405E-08
0.00235	8.97E-07	0.998106	-1.376E-08
0.00256	3.59E-07	0.998802	-1.504E-08
0.00277	3.61E-08	0.99962	-4.267E-08
0.00298	2.38E-09	0.999902	-2.254E-08
0.00349	1.97E-10	0.999972	-4.698E-08

Table 9: Entropy Generation Values with and without Energy Solver

Entropy Generation Comparisons	Weighted Variable Sum for Entropy Generation with Diffusion	Variable Sum for Entropy Generation with Diffusion
With Energy Solver	2.05E-05	4.98E+12
Without Energy Solver	2.05E-05	4.98E+12
% Difference	9.774E-06	4.017E-06

Appendix 3: Data Tables

A3.1: Non-dimensionalized x-axis values

Model coordinate values were offset by 0.0002375 in the positive x direction (the long axis of the model) from the actual coordinates of a physical version of the model, due to the 0-point of the model being inside the model, a consequence of the starting point of its creation in SOLIDWORKS. Values in the following table have corrected for that offset, so a value of 0 is on inlets and a value of 1 is on the outflow.

Table 10: Non-Dimensionalized X-Values and Their Associated Points

non-dimensionalized x-values					
Point Name	Point 1	Point 2	Point 3	Point 4	Point 5
Mixing Index	0.064881	0.114881	0.164881	0.414881	0.8875
Entropy Generation	0.064881	0.114881	0.164881	0.414881	1

A3.2: Mesh Analysis Data Tables

Mesh Info			Mass Fraction Values									
			Point 1		Point 2		Point 3		Point 4		Point 5	
Name	Nodes	Re	Variance	MI	Variance	MI	Variance	MI	Variance	MI	Variance	MI
2619	3.10E+06	1	2.17E-01	0.069	2.01E-01	0.102	1.79E-01	0.154	1.45E-01	0.239	8.90E-02	0.403
175619	4.64E+06	1	2.22E-01	0.058	2.05E-01	0.093	1.94E-01	0.120	1.50E-01	0.225	9.26E-02	0.392
15619	7.14E+06	1	2.25E-01	0.052	2.09E-01	0.085	1.97E-01	0.112	1.53E-01	0.218	9.23E-02	0.392
125619	1.23E+07	1	2.26E-01	0.049	2.11E-01	0.082	1.99E-01	0.108	1.54E-01	0.215	9.40E-02	0.387
1619	2.39E+07	1	2.20E-01	0.063	1.98E-01	0.111	1.98E-01	0.109	1.52E-01	0.220	9.48E-02	0.384
2619	3.10E+06	50	2.16E-01	0.071	1.49E-01	0.227	6.74E-02	0.481	1.41E-05	0.992	8.75E-10	1.000
175619	4.64E+06	50	2.21E-01	0.059	1.55E-01	0.213	7.63E-02	0.448	2.84E-04	0.966	1.73E-08	1.000
15619	7.14E+06	50	2.23E-01	0.056	1.61E-01	0.197	8.77E-02	0.408	2.10E-03	0.908	3.38E-07	0.999
125619	1.23E+07	50	2.25E-01	0.051	1.67E-01	0.183	9.36E-02	0.388	1.72E-03	0.917	3.17E-07	0.999
1619	2.39E+07	50	2.25E-01	0.051	1.73E-01	0.169	1.01E-01	0.363	2.72E-03	0.896	2.09E-06	0.997

Table 11: Mass Fraction Values for Mesh Analysis with Variance and Mixing Indices

Table 12: Entropy Generation Values for Mesh Analysis - Points 1-4

Entropy Generation								
Mesh Info			Point 1			Point 2		
Name	Nodes	Re	Vis	Diff	Tot	Vis	Diff	Tot
2619	3100760	1	1.40E-10	2.42E-09	2.6E-09	3.37E-10	4.79E-09	5.13E-09
175619	4636260	1	1.42E-10	2.66E-09	2.8E-09	3.40E-10	5.33E-09	5.67E-09
15619	7137994	1	1.43E-10	2.81E-09	3E-09	3.42E-10	5.60E-09	5.94E-09
125619	12329602	1	1.45E-10	3.01E-09	3.2E-09	3.46E-10	5.91E-09	6.26E-09
1619	23858769	1	1.46E-10	3.32E-09	3.5E-09	3.48E-10	6.44E-09	6.78E-09
Name	Nodes	Re	Vis	Diff	Tot	Vis	Diff	Tot
2619	3100760	50	5.69E-07	4.15E-09	5.7E-07	1.76E-06	1.03E-08	1.77E-06
175619	4636260	50	5.86E-07	4.76E-09	5.9E-07	1.81E-06	1.25E-08	1.83E-06
15619	7137994	50	5.96E-07	5.40E-09	6E-07	1.86E-06	1.46E-08	1.87E-06
125619	12329602	50	6.12E-07	6.35E-09	6.2E-07	1.91E-06	1.83E-08	1.93E-06
1619	23858769	50	6.24E-07	7.87E-09	6.3E-07	1.96E-06	2.45E-08	1.99E-06
Mesh Info			Point 3			Point 4		
Name	Nodes	Re	Vis	Diff	Tot	Vis	Diff	Tot
2619	3100760	1	5.47E-10	6.68E-09	7.2E-09	1.56E-09	1.37E-08	1.52E-08
175619	4636260	1	5.50E-10	7.33E-09	7.9E-09	1.57E-09	1.49E-08	1.65E-08
15619	7137994	1	5.54E-10	7.68E-09	8.2E-09	1.58E-09	1.55E-08	1.71E-08
125619	12329602	1	5.59E-10	8.08E-09	8.6E-09	1.59E-09	1.61E-08	1.77E-08
1619	23858769	1	5.63E-10	8.70E-09	9.3E-09	1.60E-09	1.70E-08	1.86E-08
Name	Nodes	Re	Vis	Diff	Tot	Vis	Diff	Tot
2619	3100760	50	3.16E-06	1.71E-08	3.2E-06	9.71E-06	2.33E-08	9.73E-06
175619	4636260	50	3.24E-06	2.08E-08	3.3E-06	1.00E-05	2.97E-08	1.01E-05
15619	7137994	50	3.33E-06	2.49E-08	3.4E-06	1.03E-05	3.77E-08	1.04E-05
125619	12329602	50	3.42E-06	3.22E-08	3.5E-06	1.07E-05	5.14E-08	1.07E-05
1619	23858769	50	3.51E-06	4.31E-08	3.6E-06	1.09E-05	7.51E-08	1.1E-05

Table 13: Entropy Generation Values for Mesh Analysis - Point 5

Entropy Generation, continued					
Mesh Info			Point 5		
Name	Nodes	Re	Vis	Diff	Tot
2619	3100760	1	3.13E-09	2.21E-08	2.5E-08
175619	4636260	1	3.15E-09	2.40E-08	2.7E-08
15619	7137994	1	3.17E-09	2.49E-08	2.8E-08
125619	12329602	1	3.19E-09	2.57E-08	2.9E-08
1619	23858769	1	3.21E-09	2.69E-08	3E-08
Name	Nodes	Re	Vis	Diff	Tot
2619	3100760	50	1.99E-05	2.33E-08	2E-05
175619	4636260	50	2.04E-05	2.98E-08	2E-05
15619	7137994	50	2.11E-05	3.79E-08	2.1E-05
125619	12329602	50	2.17E-05	5.16E-08	2.2E-05
1619	23858769	50	2.24E-05	7.57E-08	2.2E-05